UNCLASSIFIED

AD NUMBER

AD826125

NEW LIMITATION CHANGE

TO

Approved for public release, distribution unlimited

FROM

Distribution authorized to U.S. Gov't. agencies and their contractors; Critical Technology; JUN 1967. Other requests shall be referred to Air Force Materials Lab., Wright-Patterson AFB, OH 45433.

AUTHORITY

AFSC ltr, 2 Mar 1972

THIS PAGE IS UNCLASSIFIED

1125-1-DP145

AD826125

SPECIAL FRACTOGRAPHIC TECHNIQUES FOR FAILURE ANALYSIS

JUNE 1967

PREPARED BY

B.V. WHITESON
A. PHILLIPS
R.A. RAWE
AND
V. KERLINS
MATERIALS RESEARCH AND PRODUCTION
METHODS DEPARTMENT
MISSILE AND SPACE SYSTEMS DIVISION
DOUGLAS AIRCRAFT COMPANY

DDC

RECEIVED
FEB 5 1968

Ag 149585

SPECIAL FRACTOGRAPHIC TECHNIQUES FOR FAILURE ANALYSIS

B. V. Whiteson, A. Phillips, V. Kerlins and R. A. Rawe

Missile and Space Systems Division

ABSTRACT

In order to assist the investigator of service failures, work was performed using electron fractographic methods to resolve problems that have not been solvable using the more conventional macro- or light microscope techniques. Three independant problems were examined, and solutions were achieved. These were:

1. Determination of fracture direction in thin sheet metal components.

2. Differentiating between hydrogen embrittlement and stress corrosion in high strength steels.

3. Determination of applied cyclic stress as a function o. fatigue striation spacing.

The results of the investigation indicated that:

1. Fracture direction in thin sheet metal components can be resolved by the combined technique of replicating around the acute angle shear lip of the fracture face and the sheet metal face, and the use of low magnifications on the electron microscope. The direction of tear dimples with respect to the fracture edge consistently indicated the fracture direction in the plane of fracture propagation.

2. There is reasonable evidence that stress corrosion and hydrogen embrittlement in high strength steel can be separated by the following:

   a. Hydrogen embrittlement fractures initiated subsurface, while stress corrosion fractures initiated on the free surface.

   b. Stress corrosion fractures had indications of secondary cracking while hydrogen embrittlement failures did not.

   c. The fracture features on the hydrogen embrittlement specimens were clearer than those on the stress corrosion fractures.

3. A correlation was established between cyclic stress and fatigue striation spacing for several aluminum alloys over a wide range of alternating and mean stresses in thicknesses of 0.050 and 0.500-inches. The correlation was empirically derived and is of the form:

$$\sigma_a = \left[\frac{P}{\sigma_m^{1/3}} \frac{\log (\ell/w)}{\log (s/S_w)} \right]^2$$

A relationship of the form

$$\frac{d}{dn} = \frac{(\Delta K)^4}{M}$$

did not prove adequate to describe the data in this investigation due to the fact that M appeared to be stress dependant.

CREDIT

KEY WORDS

Electron Microscope

Electron Fractography

Failure Analysis

Fracture

Fracture Direction

Replication Methods

Hydrogen Embrittlement

Stress Corrosion

Fatigue

Striation Spacing

Crack Propagation Rates

Fracture Toughness

Fatigue Testing

Aluminum

Steel

Waspalloy

Sustained Load Testing

Dimpled Fractures

Intergranular Fracture

Cadmium Plating

High Strength Materials

PROBLEM 1.   Determination of Fracture Direction

in Thin Sheet-Metal Components

Introduction

In service failure analysis, an extremely important aspect of the
investigation usually centers around locating the origin or nucleus of
the fracture. Generally the fracture origin holds the key to the reason
for failure and also paves the way for corrective action. If the origin
is not clearly identifiable visually, the most common method of locating
it is to trace the fracture direction on the failed components back to
a common intersection point. The ability to trace fracture direction
on the failed components generally depends on macroscopic features
such as chevron marks, localized zones of plane strain, hackle marks, [1]
etc. This task becomes difficult, if not impossible, when the fracture
is all oblique shear, which is usually the case with relatively thin,
ductile materials that are used in the skins of aircraft and the fuel
tanks of missiles and launch vehicles. In this case there are no
macroscopic features that are clearly identifiable with fracture
direction, much to the frustration of the investigator.
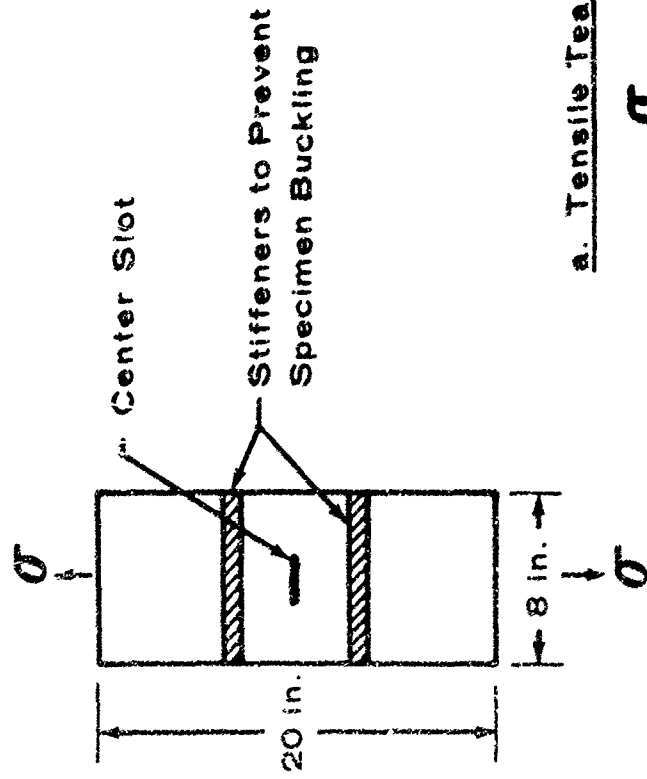
The purpose of this work was to find out if the electron microscope
could provide a method to determine fracture direction in thin sheet-
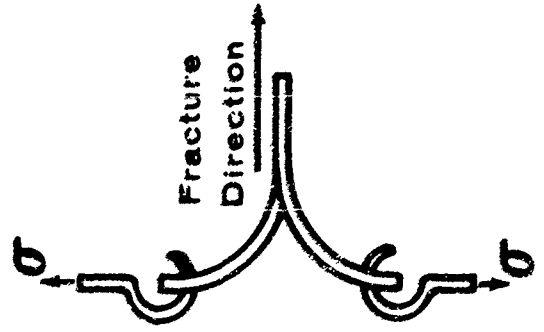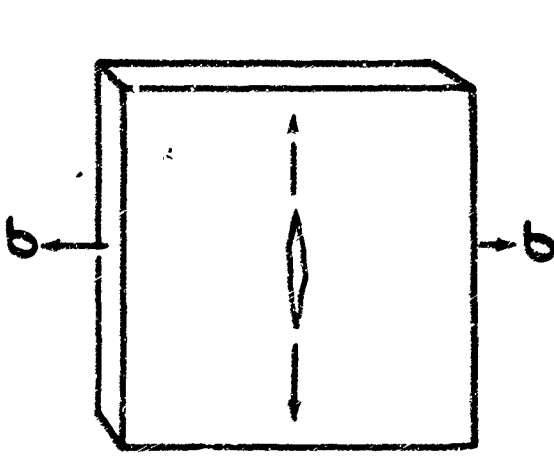metal components.

Experimental Procedure

Materials and thicknesses were typical of those generally used in
aircraft and missiles (Table 1). Two types of specimens were tested
in order to obtain a tensile tear (Figure 1a) and a combined shear and

TABLE 1--MECHANICAL PROPERTIES AND THICKNESSES OF METALS USED FOR FRACTURE DIRECTION DETERMINATION

Material	Thickness, In.	Strength	
		F_{ty}, ksi	F_{tu}, ksi
4340 Steel	0.050	207.7	260.7
4340 Steel	0.050	170.3	184.8
4340 Steel	0.125	215.5	270.3
4340 Steel	0.125	174.7	187.4
D6AC Steel	0.050	247.4	288.3
D6AC Steel	0.125	252.1	293.6
AM350 Steel	0.050	174.7	202.5
AM350 Steel	0.125	171.9	204.5
7075-T6 Aluminum	0.050	75.9	83.9
7075-T6 Aluminum	0.125	78.5	84.5
2024-T3 Aluminum	0.050	51.5	69.5
2024-T3 Aluminum	0.125	56.6	71.8
7079-T6 Aluminum	0.050	64.9	72.0
7079-T6 Aluminum	0.125	64.9	72.0
Waspelloy	0.050	125.3	185.8
Waspelloy	0.125	130.7	188.0

Stiffeners to Prevent
Specimen Buckling

Center Slot

20 in.

8 in.

2 in.

2 in.

1 in.

a. Tensile Tear Specimen

Fracture
Direction

b. Combined Tear & Shear Specimen
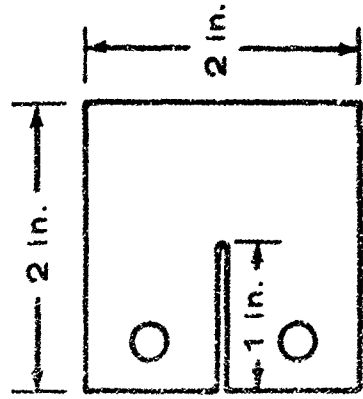
tear fracture (Figure 1b). All materials failed with fractures that had 100 percent oblique shear, Figure 2, with no areas of plane strain that provided any macroscopic indication of fracture direction.

Results

In all specimens fracture direction was discerible using the electron microscope, and it is believed that the technique for determining fracture direction is applicable to all materials that fail by dimple rupture[2]. For simplicity, none of the individual materials tested are delineated in the illustr ions, since the fractographic features analyzed are identical, except for the relative size and abundance of the observed dimples.

The basic concept of determining fracture direction that applies to all materials which fail by dimple rupture is illustrated in Figure 3. For all specimens tested, the open elongated dimples (dimples with the open end of their parabolas toward the fracture edge) along the edge of the rupture point back to the fracture origin (Figure 3a). The open dimples occur predominantly on the acute angle shear lip. The closed elongated dimples (dimples with the closed ends of their parabolas toward the fracture edge) along the obtuse angle shear lip and those found in the center of the fracture were usually randomly oriented and could not be used for fracture direction determination (Figure 3b and 3c).

The acute angle shear lip was replicated by the plastic-carbon technique[2] in such a way as to overlap the edge of the fracture. In order to orient the replica with respect to the fractured specimen, one or both corners of a rectangular replica were cut so as to indicate the
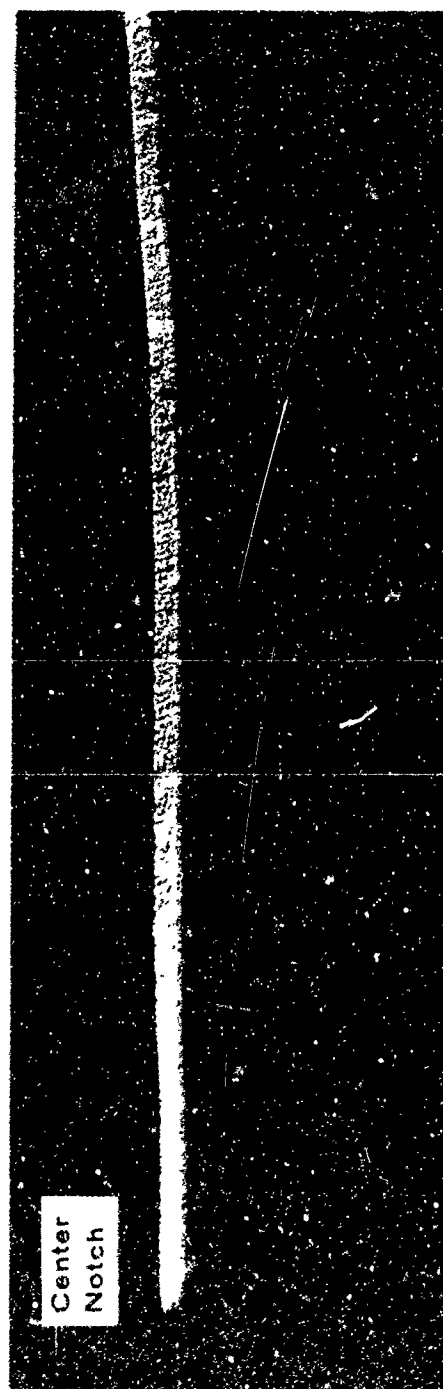
Tensile Tear Specimen (fracture direction →)
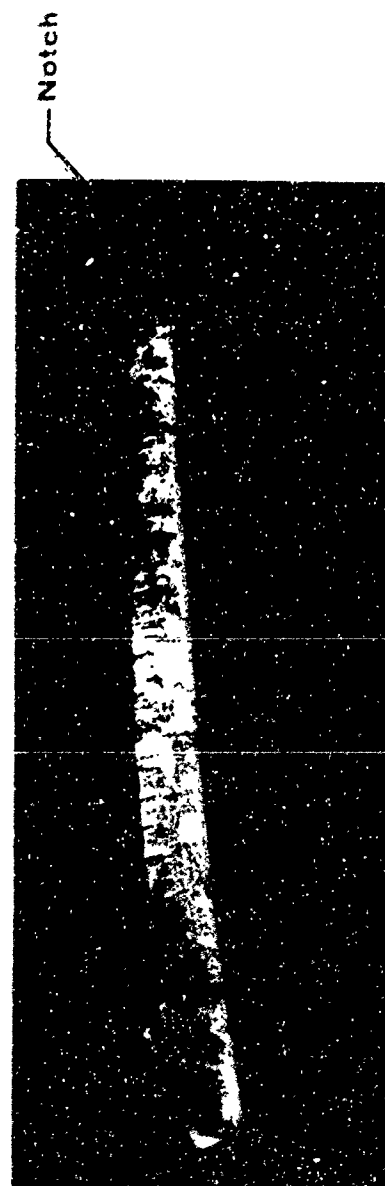
Tear & Shear Specimen (fracture direction ←)

Figure 2. The Appearance of the Fracture Surfaces of Tensile Tear and Tear & Shear Specimens
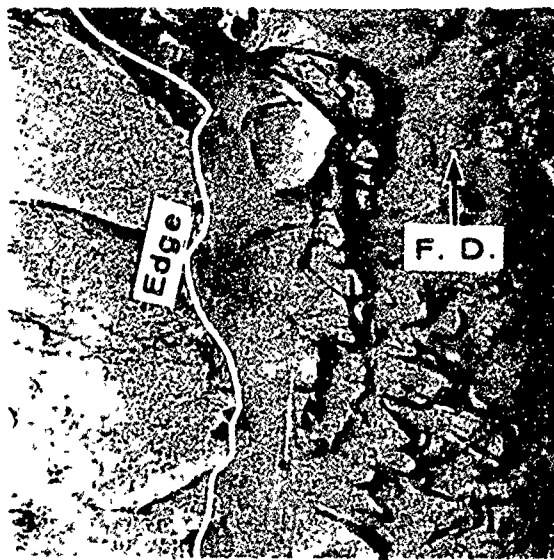
(a)   Magn. 6200X   (b)   Magn. 6200X
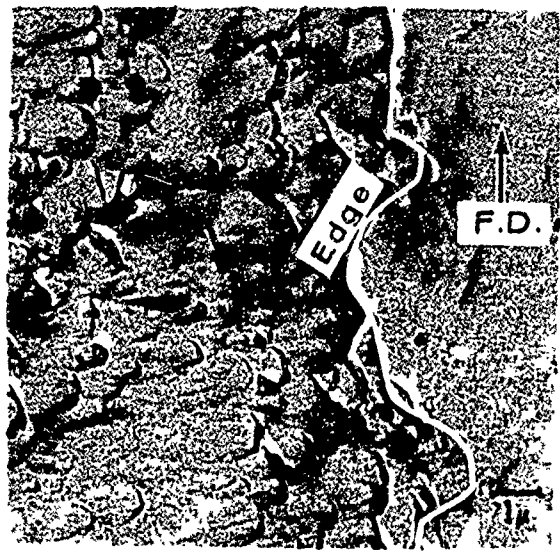
Open Dimples   **Closed Dimples**

F.D. = Fracture Direction
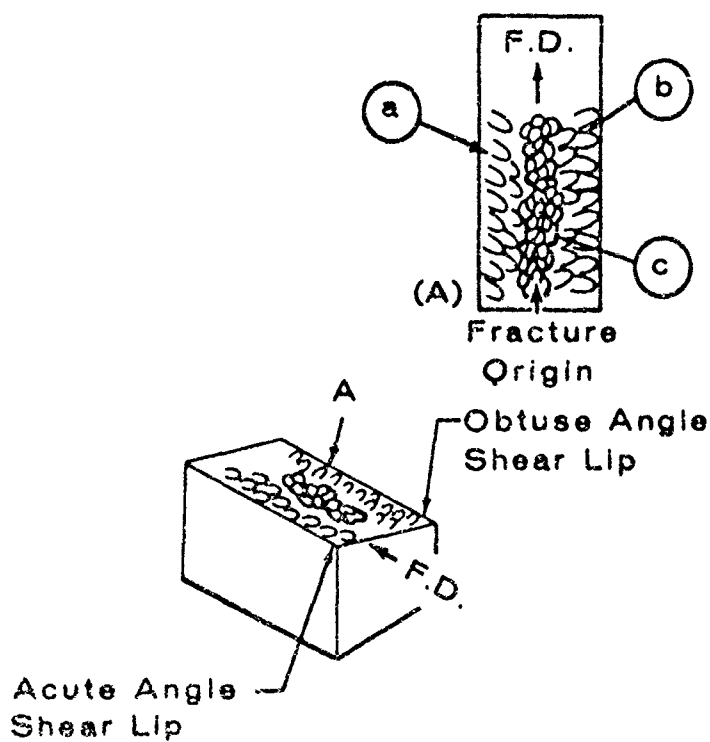
(c)   Magn 3500X

Equiaxel Dimples

Figure 3. Relationship Between Orientation of Open Dimples Along Fracture Edge and Fracture Direction

6

desired orientation. The replica was then placed in the electron microscope so that the replica orientation with respect to the fracture could be maintained in the electron fractograph. The fracture direction was then related back to the actual specimen. The complete t 'nique is illustrated in Figure 4.

It was very important to obtain a good replica of the fracture edge and the open dimples immediately adjacent to it. This was essential because the orientation of the open dimples had to be determined locally with respect to the edge. In order to obtain an accurate indication of the edge line, low magnification (approximately 500X) electron microscopy techniques were used. A series of overlapping electron fractographs were taken along the edge region in order to obtain an accurate sense of the dimple direction. A typical low magnification electron fractograph showing open dimples along a fractured edge is shown in Figure 5.

Discussion

The sensitivity of dimples to fracture direction can be explained by considering the basic difference between shear and tear dimples. In case of a "pure" shear fracture, the dimples point in opposite directions on mating fracture surfaces[2]. In case of a "pure" tear, the dimples point in the same direction (back to the fracture origin) on both mating fracture surfaces. Since from a practical standpoint no fracture occurs by "pure" shear alone, i.e., some tearing always accompanies a running fracture in thin sheet material, the resulting elongated dimples observed on a fracture surface are the end product of a combined shear and tear

7

Fracture Surface

Arbitrary Surface
Replica Reference
Direction

Surface

Plastic Replica

Fracture — — Fracture Edge

— Surface

STEP 1

STEP 2

— Cut to Identify Replica
Reference Direction
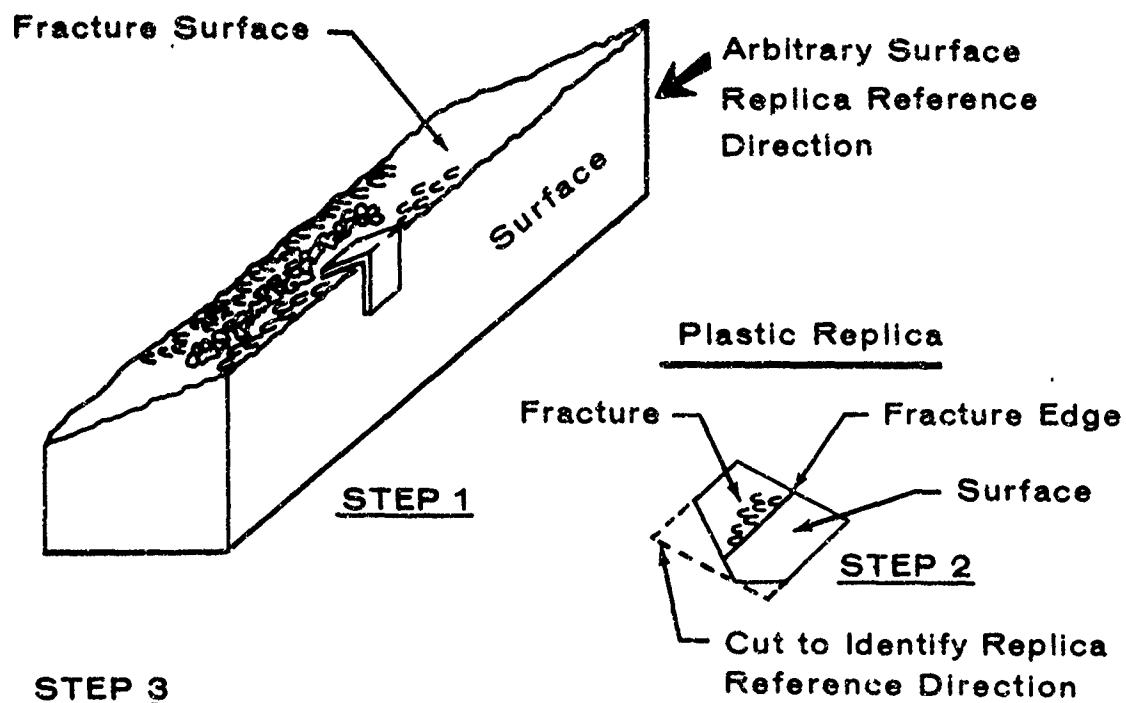
STEP 3

Shadow and Deposit Carbon by Normal
Two Stage Plastic—Carbon Technique.

Figure 4. Fracture Direction Replication Technique.

8
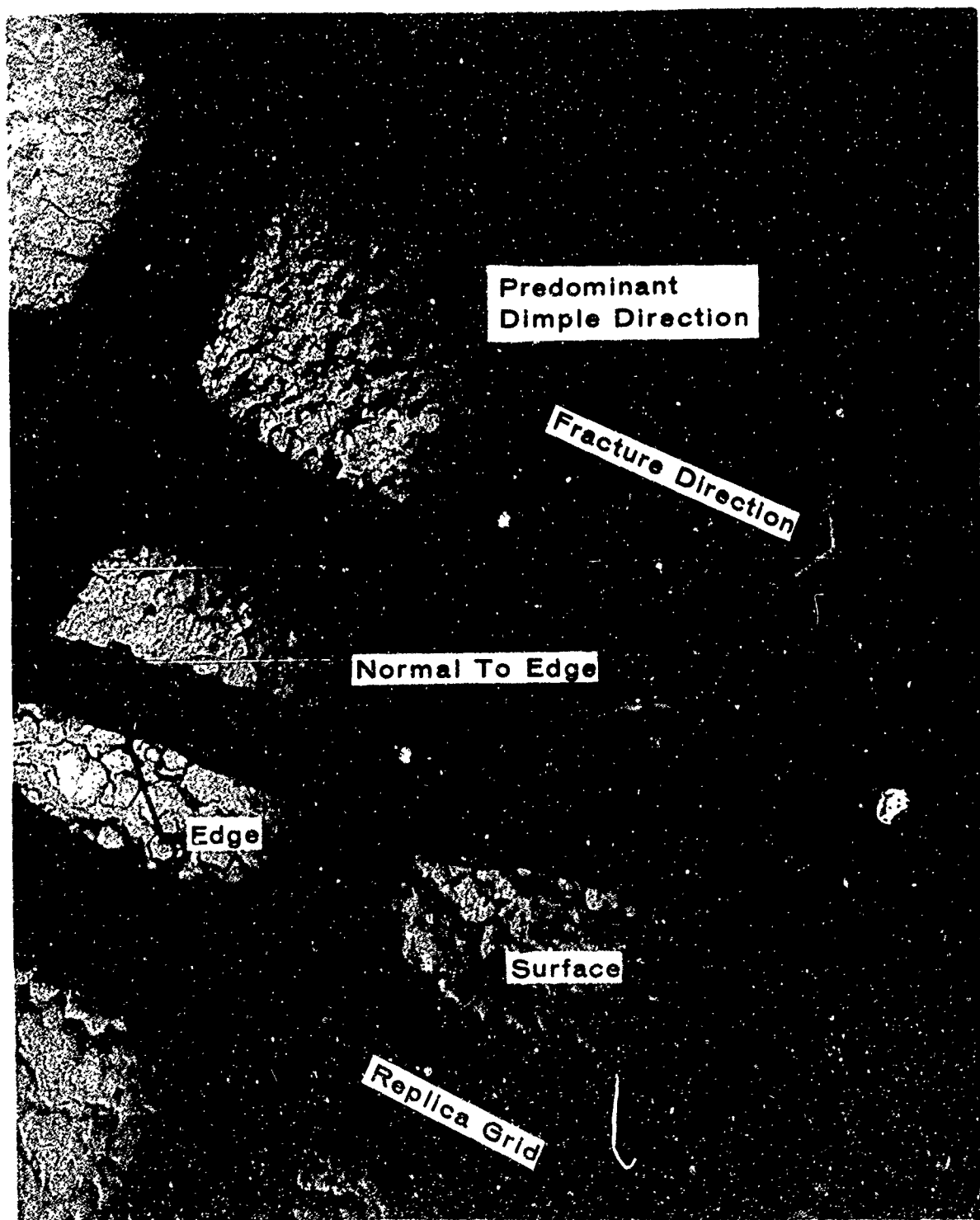
Magn. 400X

Figure 5. Open Dimples Along Fracture Edge Indicate
Fracture Direction

type of fracture. If a fracture propagates prediminantly by a tear mechanism, the elongated dimples would point more strongly in the direction of fracture origin than if it propagated primarily by a shear mechanism. This concept of resultant combined dimples is illustrated in Figure 6.

It is not clear, however, why open dimples are consistent in their orientation with respect to fracture direction while closed dimples have shown inconsistency. Assuming that a fracture separation can be non-symmetrical, it is difficult to explain why this non-symmetry should only affect closed dimples since their apparent "twin" is an open dimple which is oriented in a systematic and orderly fashion. Perhaps discontinuous propagation at the center of the fracture (voids occurring ahead of the crack front) could account for the lack of orderly dimple orientation in this region.

Conclusions

1. It is possible to determine fracture direction in thin sheet-metal that fails in an oblique shear mode, and by dimpled rupture, by observing the orientation of open dimples along the fracture edge at the acute angle shear lip.

2. Replicas must be taken that overlap the fracture surface and the sheet metal face, coupled with low magnification microscopy, in order to obtain an accurate assessment of the open dimple orientation with respect to the fracture edge.

3. The type of material examined is not important, as long as dimples are visible on the fracture surface.

10
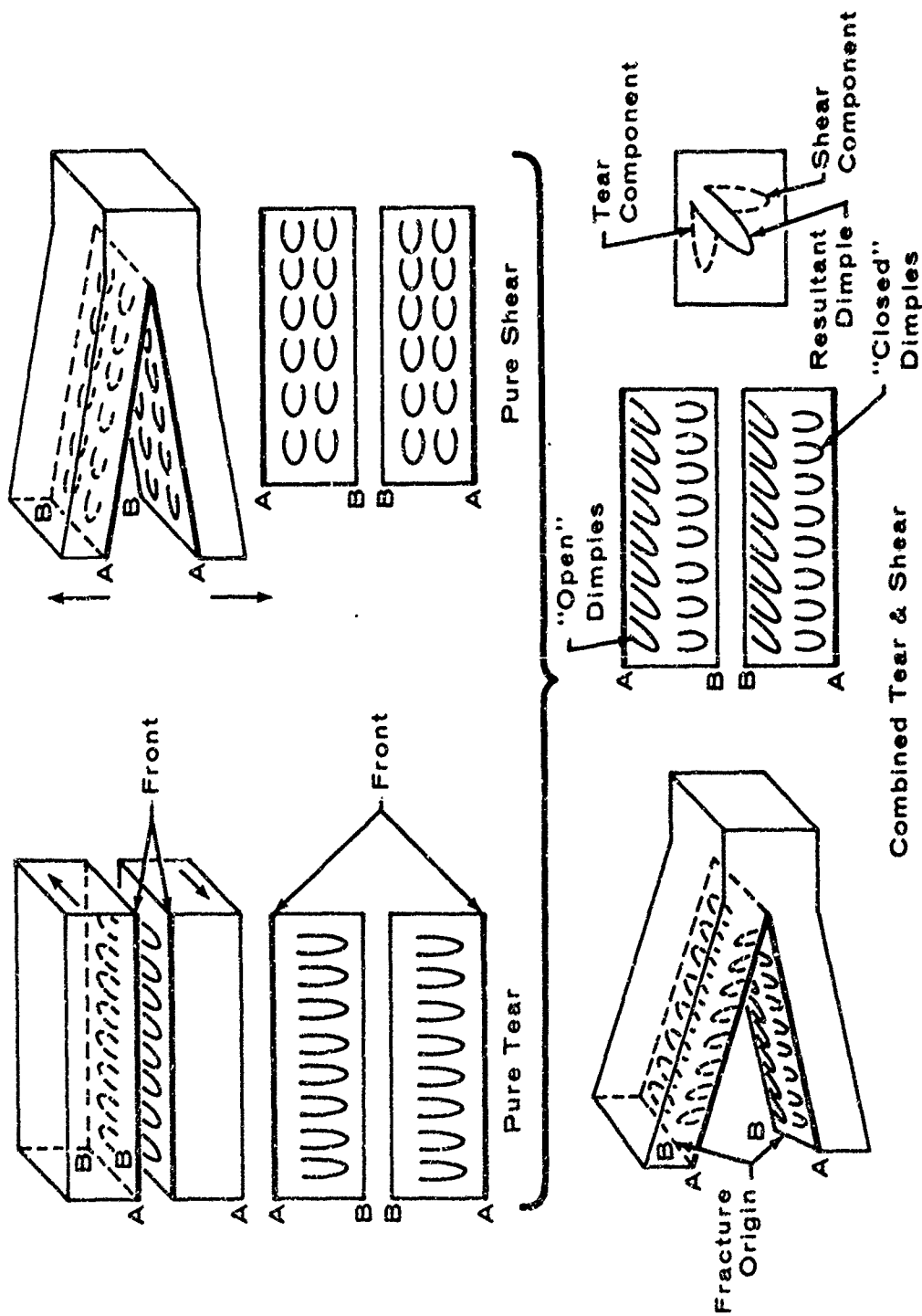
Figure 6. Relationship Between Open Dimple Orientation and Fracture Origin

PROBLEM 2--Electron Fractographic Technique for Distinguishing Stress

Corrosion From Hydrogen Embrittlement in High Strength Steels

Introduction

Stress corrosion and hydrogen embrittlement have been a common and
exceptionally perplexing source of service failures in the high strength,
medium-carbon, low-alloy steels. These fractures most commonly occur on
components that have long life spans and exist under some level of sus-
tained stress even when the component is not in use. There have been
attempts to distinguish between the appearances of the fractures caused
by stress corrosion and hydrogen embrittlement without substantial
success because the two failure types exhibit a remarkably similar
fracture appearance[2]. It would be of great importance in failure
analysis to have the ability to recognize differences in the fracture
appearances of the two failure mechanisms so that appropriate corrective
action can be taken.

Experimental Procedure

Sustained load tests were conducted to produce failures due to stress
corrosion or hydrogen embrittlement. The alloys selected were forged
4340, 4330M and D6AC. The mechanical properties are shown in Table 2.
The sustained load specimen configuration is shown in Figure 7.

TABLE 2--MECHANICAL PROPERTIES OF STEELS USED FOR

HYDROGEN EMBRITTLEMENT AND STRESS CORROSION TESTS

Material	Thickness, in.*	Strength	
		F_{tu}	F_{ty}
4340	0.050	277.2	240.9
4330M	0.050	224.4	193.8
D6AC	0.050	289.6	243.2

*Cut from 4-1/2" square billet in the transverse grain direction

To evaluate hydrogen embrittlement, three distinct cadmium plating processes were used to provide qualitative differences in the hydrogen levels in the test specimens:

    1. Acid pickle plus cadmium fluoborate plating

    2. Bright cadmium cyanide plating

    3. Cadmium fluoborate plating.

All plating conformed to the requirements of QQ-P-416, except that specimens were not embrittlement relief baked after plating. This was done to insure specimen failure. The stress corrosion specimens were tested in the bare and vacuum cadmium plated condition (MIL-C-8837). Both hydrogen embrittlement and stress corrosion tests were conducted at 50, 75 and 90 percent of yield strength. Specimens were axially loaded in the spring jigs shown in Figure 8. The hydrogen embrittlement tests were conducted in plastic bags containing silica gel

13
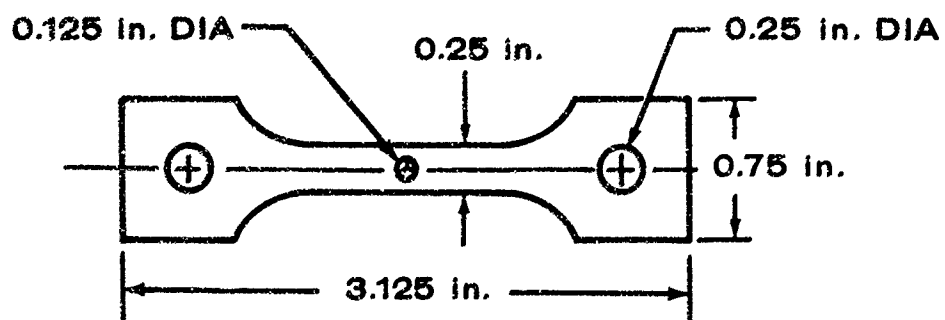
Figure 7. Configuration of Hydrogen Embrittlement and
Stress Corrosion Specimens
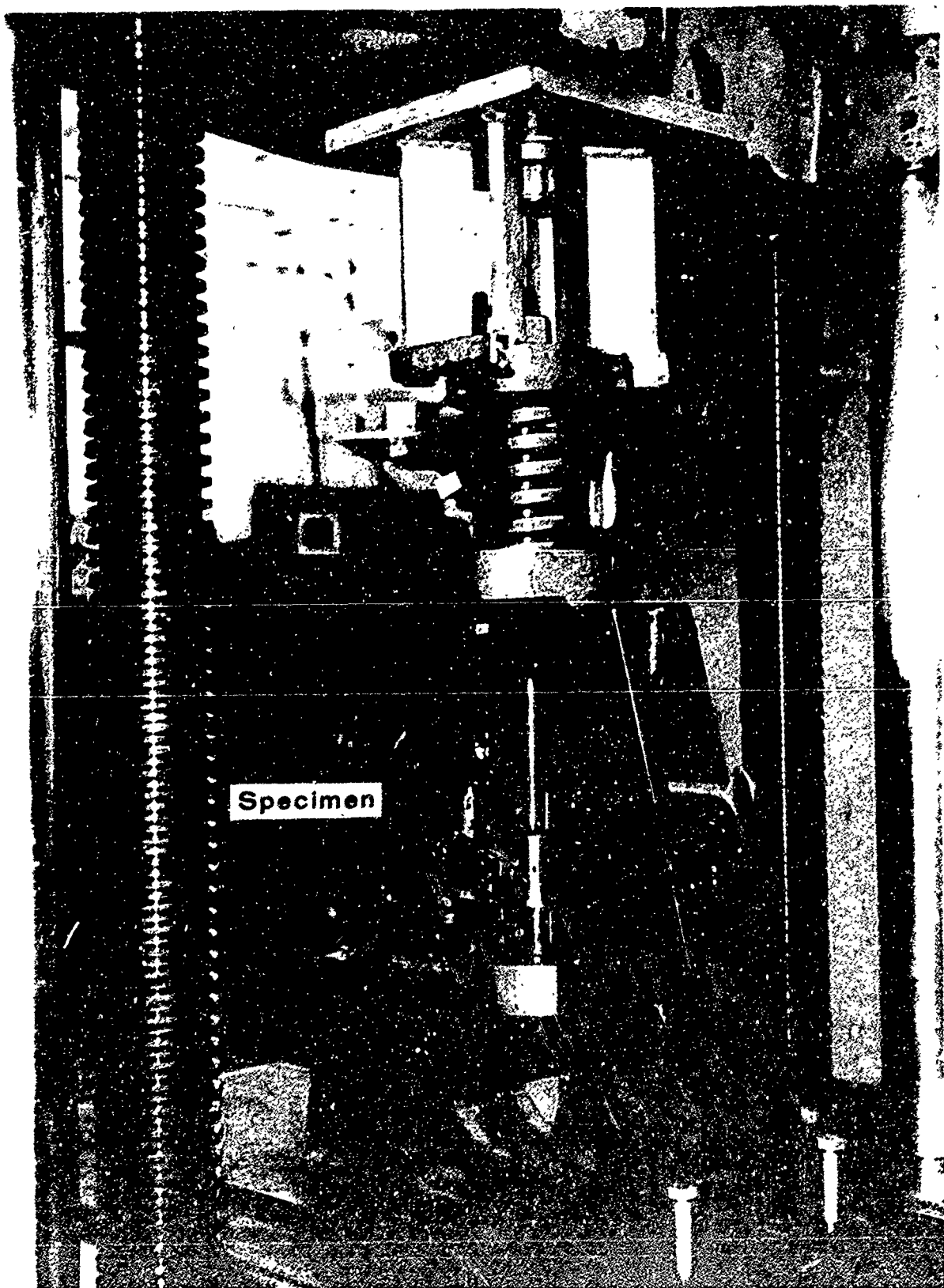
Figure 8. Specimen Jig Being Loaded in a Tensile Machine

desiccant. The stress corrosion tests were conducted by alternate immersion in deionized water (10 minutes in water, 50 minutes in air).

Results

The electron fractographic examination of known stress corrosion and hydrogen embrittlement fractures revealed similar characteristics for the steels examined, and it appeared that no exclusive single feature precisely identifies either fracture mechanism. However, a combination of features could be used to distinguish between the two types of failure. The features associated with stress corrosion fracture were:

1. Predominantly surface nucleation of intergranular fracture.

2. Intergranular regions show pronounced secondary cracking or deep crevices.

3. A relatively greater amount of oxidation or corrosion attack at the nucleus and slow growth region than in the rapid fracture area.

4. Less pronounced hairline indications on the intergranular surfaces of stress corrosion fractures in comparison to intergranular surfaces of hydrogen embrittlement fractures.

The features associated with hydrogen embrittlement were:

1. Predominantly sub-surface nucleation of intergranular fracture.

2. Evidence of partial dimples and distinct hairline indications in the intergranular regions.

3. Both the nucleus and the rapid fracture areas exhibit relatively equal degrees of oxidation or corrosion products.

In order to determine whether a fracture nucleus was surface or sub-surface, a two stage plastic-carbon replication technique was used. The suspected nucleus region was marked by placing a fine scribe line on the free surface next to the nucleus area. The plastic replica was allowed to overlap the edge so as to include the scribe line on the free surface. This line was then used as a guide to locate the nucleus area. The differences between the nucleus regions of stress corrosion and hydrogen embrittlement fractures are shown in Figure 9. In the case of stress corrosion, the intergranular nucleus area followed the surface and extended straight back from the surface. In the case of hydrogen embrittlement, the intergranular nucleus region formed predominantly sub-surface.

Other features associated with each type of fracture are shown in Figure 10. Stress corrosion usually showed evidence of secondary cracking and corrosion products in the nucleus region. The hairline indications in the intergranular regions and partial dimples which are thought to be associated with the fracturing process are somewhat more distinct in hydrogen embrittlement than in stress corrosion fractures. These subtle differences are illustrated in Figure 11.

By using a microautoradiographic technique[3], it was shown that hydrogen was associated only with the intergranular portion of the fracture. Due to the relatively low resolution of the technique, it was not possible to relate hydrogen accumulation at specific structural details such as partial dimples or hairline indications.

17
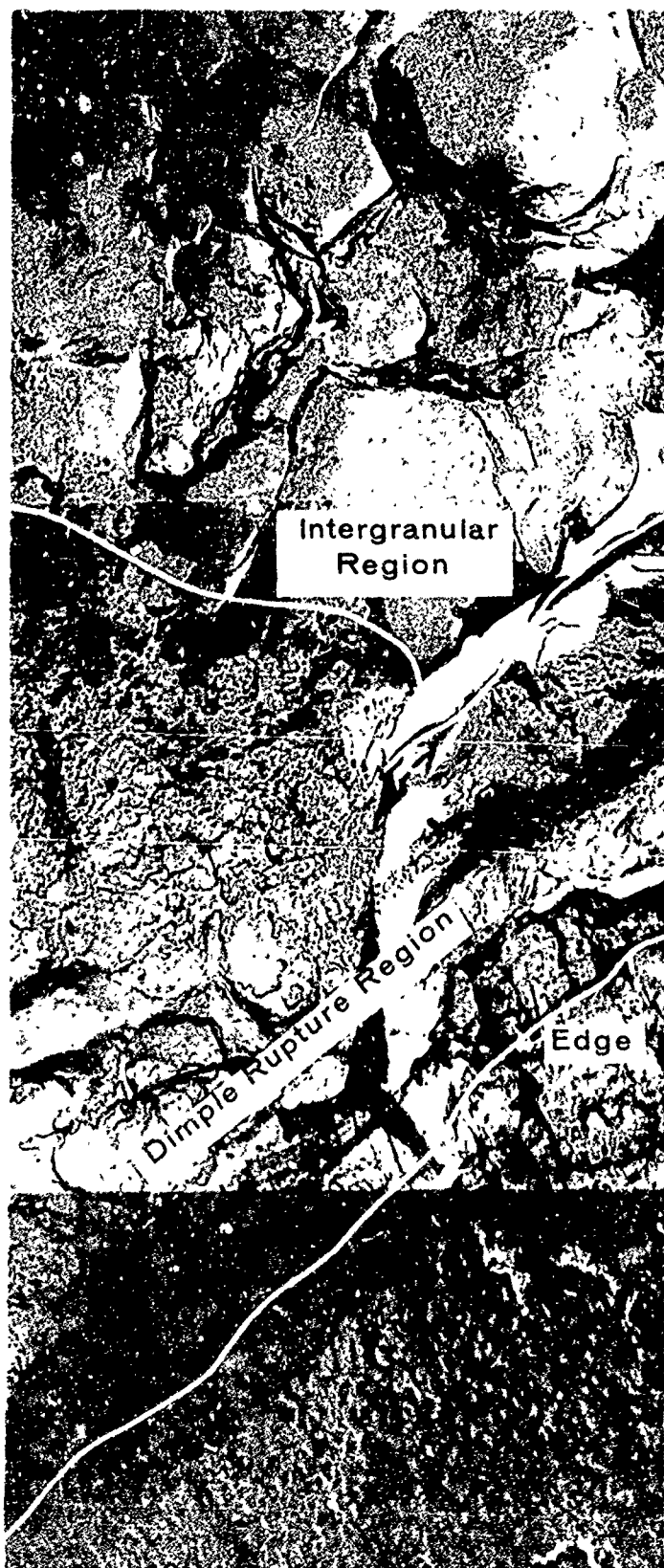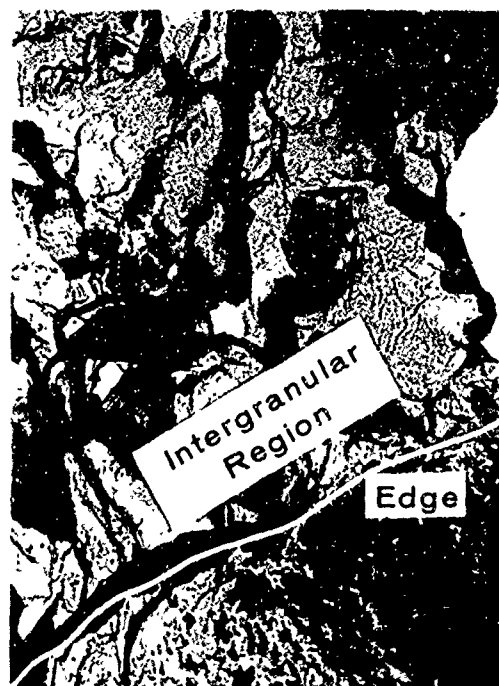
Magn. 2000X
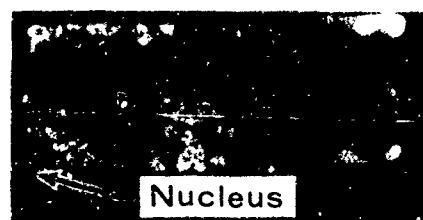
Stress Corrosion
Magn. 16X
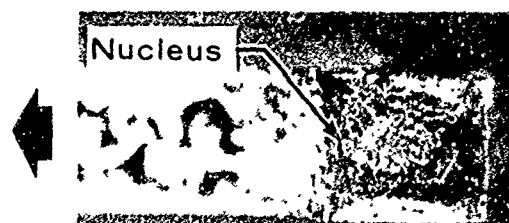
Hydrogen Embrittlement
Magn. 16X

Magn. 3500X

Figure 9. The Nature of Nucleus Region For Stress
Corrosion and Hydrogen Embrittlement Fractures

Stress Corrosion — Corrosion Products (Arrows)

Hydrogen Embrittlement — Partial Dimples (Arrows)

Stress Corrosion — Secondary Cracks and Crevises (Arrows)

Hydrogen Embrittlement - Hairline Indications (Arrows)

Figure 10. Typical Electron Fractographs Showing The Distinguishing Features of Stress Corrosion and Hydrogen Embrittlement Magnified 6,500X

19
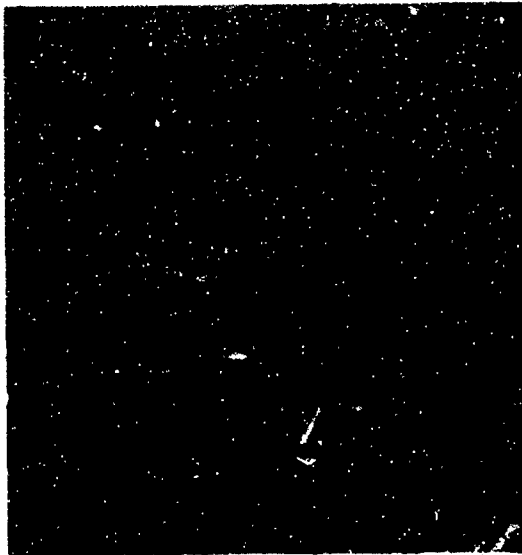
Hydrogen Embrittlement

Stress Corrosion

Hydrogen Embrittlement

Stress Corrosion

Figure 11. Illustration of Subtle Differences Between Hairline
Indications (Arrows) of Stress Corrosion and Hydrogen
Embrittlement Fractures in 4340, 260/280 Steel,
Magn. 6500X

Discussion

It has been shown that the accumulation of hydrogen with accompanying crack nucleation occurs at a region of high triaxial state of stress[3 and 4]. This triaxial state of stress exists sub-surface at the root of a notch; therefore, it is not unexpected to find evidence of sub-surface nucleation in hydrogen embrittlement fractures. In stress corrosion fractures, however, surface nucleation occurs because corrosion initiates from the surface and progresses into the material.

Intergranular fracture is associated with both stress corrosion and hydrogen embrittlement failures, and is generally confined to the nucleus region. Hydrogen embrittlement intergranular fracture showed a preponderance of partial dimples and hairline indications on the grain boundary surfaces. This suggests that a large degree of mechanical separation has been involved, whereas stress corrosion fractures, disregarding corrosion products with their accompanying surface attack, show smoother intergranular surfaces, thereby suggesting a high degree of non-mechanical separation (Dissolution).

When attempting to distinguish stress corrosion from hydrogen embrittlement fractures it was important to obtain a good overall impression of the nucleus area. Often, the differences between these two failure types were subtle and examining only a few isolated areas might have lead to incorrect analysis.

In addition, because of the subtlety between these two sustained load failure appearances, we must make use of all the far s available. This includes knowledge of the part processing practices, service history,

21

and prior service failures of the same type. The electron microscope should be used primarily to supplement knowledge rather than be the only source of information when analyzing this type of failure.

Conclusions

The features associated with stress corrosion fracture are:

1. Predominantly surface nucleation of intergranular fracture.

2. Intergranular regions show pronounced secondary cracking or deep crevices.

3. A relatively greater amount of oxidation or corrosion attack at the nucleus and slow growth region than in the rapid fracture area.

4. Less pronounced hairline indications on the intergranular surfaces than observed on hydrogen embrittlement fractures.

The features associated with hydrogen embrittlement are:

1. Predominantly sub-surface nucleation of intergranular fracture.

2. Evidence of partial dimples and pronounced hairline indications in the intergranular regions.

3. Both the nucleus and the rapid fracture areas exhibit relatively equal degrees of oxidation or corrosion products.

PROBLEM 3--Relationship Between Cyclic Stress and

Fatigue Striation Spacing

Introduction

Fatigue cracking in metal alloys is one of the most commonly observed modes of structural failure in the aerospace industry. It occurs as a result of the repeated application of loads well below the ultimate strength of the material. When the fracture surface of a fatigue crack is examined at high magnification by means of electron microscopy, periodic markings, known as striations, are observed. The spacing between striations is characteristic of the microscopic progression of the crack front during one loading cycle.

The major objective of this program was to develop a correlation between the striation spacings and the cyclic load history of through-the-thickness fatigue cracks in various sheet and plate aluminum alloys. Such a correlation would then be useful in the analysis of fatigue failures of structures fabricated from these alloys.

Experimental Procedure

The aluminum alloys studied included 2024-T3, 7075-T6, 7075-T73, 7079-T6 and 6061-T6, Table 3. For the purpose of detecting an effect of material thickness on the properties to be studied, both 0.050-in. sheet and 0.500 in. plate of 2024-T3, 7075-T6, and 7075-T73 were used. The remaining alloys were tested in the 0.050-in. thickness only.

Fatigue cracks were developed in 8-in. wide by 18-in. long specimens, centrally slotted and fatigue-precracked, Figure 12. Growth of the fatigue

TABLE 3--MECHANICAL PROPERTIES OF ALUMINUM ALLOYS
USED FOR CRACK PROPAGATION TESTS

Material	Thickness, in.	Strength	
		F_{ty}, ksi	F_{tu}, ksi
2024-T3	0.050	51.2 51.0 52.4	69.5 69.4 69.6
2024-T3	0.500	56.0 56.6 56.4	66.0 66.6 66.6
7075-T6	0.050	75.6 76.1 76.1	83.5 84.3 84.1
7075-T6	0.500	75.6 74.7 78.2	82.4 82.0 84.3
7075-T73	0.050	66.9 67.8 65.8	77.7 78.5 76.6
7075-T73	0.500	63.8 64.1 62.0	73.7 74.2 73.0
7079-T6	0.050	65.7 64.6 64.4	71.8 72.0 72.0
6061-T6	0.050	42.1 42.0 42.3	47.4 47.4 47.6

18 in.

Machined Starter Notch

Precracked by Fatigue

8 in.

Figure 12. Fatigue Crack Propagation Specimen

crack was monitored visually and by means of 2-in. long crack propagation gages bonded on one specimen surface in the path of the growing crack, Figure 13. Each gage consisted of twenty elements, equally spaced at 0.10-in. intervals. Sequential rupture of gage elements by the propagating crack was recorded by an oscillograph simultaneously with the output from the load cell. The oscillographic trace provided a detailed loading and cracking history of each specimen.

The cyclic stresses which were employed were selected to represent loading environments encountered in military aircraft and to provide evidence of the effect on striation spacing of mean stress, alternating stress, frequency of loading and material thickness.

The cyclic stresses for fatigue crack propagation tests are presented in Table 4. Standard fatigue crack propagation (Table 4a) was established in tests with constant mean and alternating stresses. In each of these tests one of the four scheduled mean stresses and one of the five scheduled alternating stresses characterized the cyclic stress for that test. The loading frequency for these tests was 1000 cycles per minute. In several tests, a frequency of 10 cycles per minute was employed.

Spectrum-load fatigue crack propagation tests (Table 4b) were also performed in order to simulate service conditions and duplicate single mean or alternating cyclic loads. In one series of these tests the mean stress was held constant while the alternating stress varied every ten cycles. In the second series, the alternating stress was held constant and the mean stress was varied every ten cycles. These tests were performed at a frequency of 600 cycles per minute.

sbt 630
cont.125
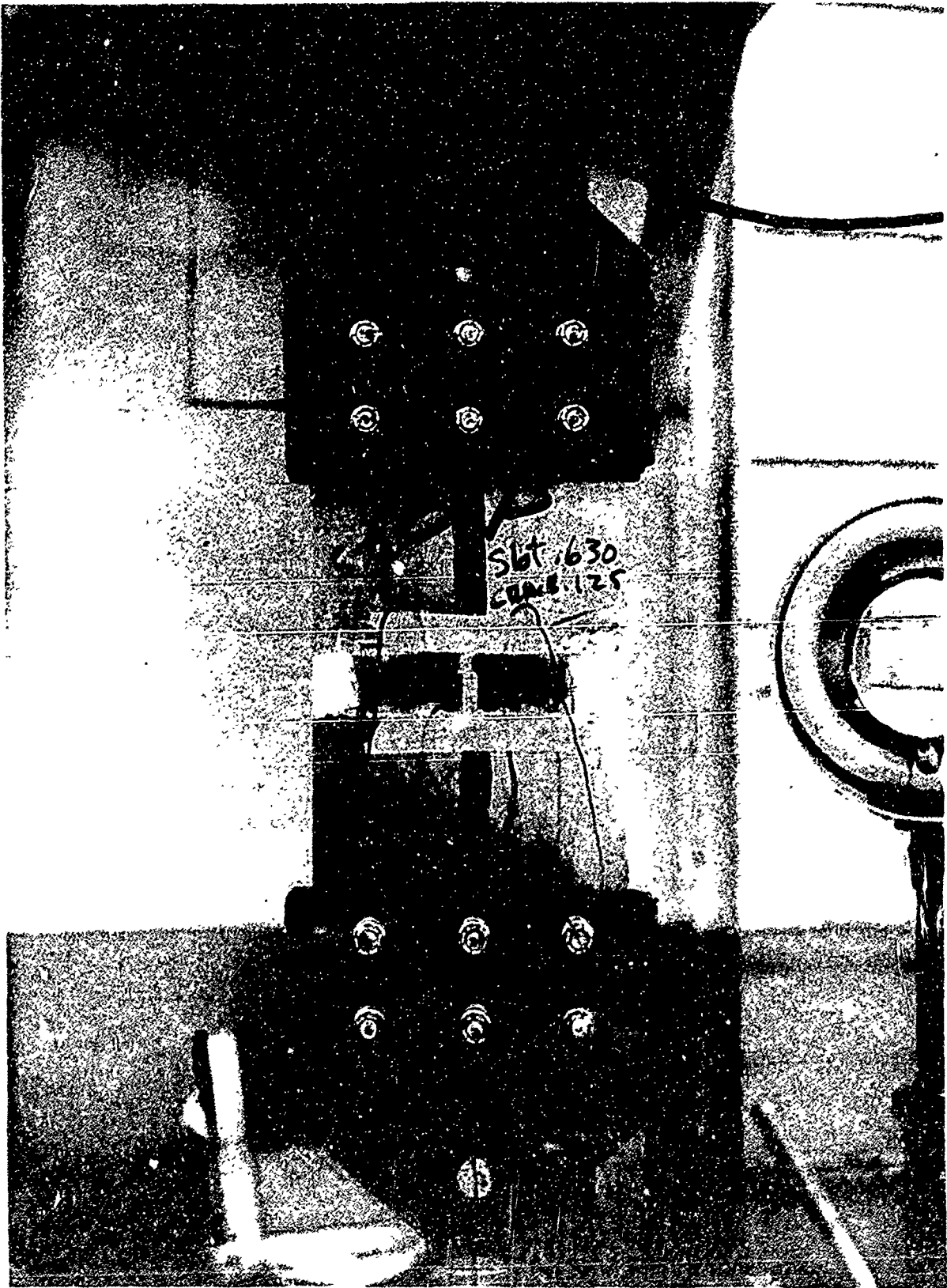
TABLE 4--FATIGUE CRACKING TEST CONDITIONS

Table 4a--Standard Fatigue Crack Propagation

Alloy	Thick. in.	Freq. cpm [4]	σ_m, ksi [1,2] 8.25	13.75	13.75	13.75	16.5	22.5
			σ_a, ± ksi [3] 6.75	2.5	7.5	11.25	13.5	6.75
2024-T3	0.050	1000	X	X	X	X	X	X
		10			X	X		
	0.500	1000		X	X	X		
7075-T6	0.050	1000	X	X	X	X	X	X
		10			X	X		
	0.500	1000		X	X	X		
7075-T73	0.050	1000	X	X	X	X	X	X
		10			X	X		
	0.500	1000		X	X	X		
7079-T6	0.050	1000	X	X	X	X	X	X
6061-T6	0.050	1000	X	X	X	X	X	X

Table 4b--Spectrum-Load Fatigue Crack Propagation

Alloy	Thick. in.	Freq. cpm	σ_m, ksi 13.75	13.75	13.75	8.25	13.75	22.5
			σ_a, ± ksi 2.5	7.5	11.25	6.75	6.75	6.75
2024-T3	0.050	600		X			X	
7075-T6	0.050	600		X			X	
7075-T73	0.050	600		X			X	
7079-T6	0.050	600		X			X	
6061-T6	0.050	600		X			X	

(1) All Stresses Based on Gross Area

(2) σ_m = mean stress

(3) σ_a = alternating stress = $\dfrac{\sigma_{max} - \sigma_{min}}{2}$

(4) Frequency in cycles per minute

The standard two-stage plastic-carbon technique was used in preparing replicas of the fatigue crack surfaces for examination in the electron microscope. A corner was cut off on each replica in order to orient it with respect to the macroscopic crack propagation direction. Striation spacings were measured from electron fractograph negatives taken at a standard magnification of 5300X. Calibration of this magnification was accomplished using a replica of a diffraction grating containing 28,600 lines per inch.

The fatigue cracks examined ranged from approximately a total length of 0.7 to 4.3 inches. The selection of areas to be replicated on individual specimens was based on the number of cycles used to propagate the left or right crack front 0.10 inches. Since it was difficult to observe distinct fatigue striations in areas where less than about 200 cycles were used to grow the fatigue crack 0.10-in., these areas were not replicated. For 0.10-in. increments containing more than 200 cycles of stress, replicas were taken at significant intervals (usually 3 to 4) along the fracture path.

The fatigue striation spacing data was obtained by examining a specific 0.10-in. area to gain an impression of representative striation spacings in this area. Generally, a fatigue striation spacing for a specific area represents an average of four readings, depending on the definition and number of striations present. Where possible, measurements were taken from relatively flat regions that exhibited the largest uniform striation spacings over an appreciable distance. Striations that were influenced by second phase particles, or occurred on steep

slopes were not considered. It was found that distinct fatigue striations could be observed on both the normal and oblique mode of the macroscopic fracture profile in the fatigue region.

Results

Completely detailed data from all the tests may be found in Appendix I.

When comparing the macroscopic fatigue crack growth rate (obtained by dividing the observed 0.10-in. increment crack growth by the number of cycles used to propagate the crack through that increment) to the microscopic growth rate (striation spacing), the following behavior was observed:

1. Macroscopic rate was less than the microscopic rate
2. Macroscopic rate was equal to the microscopic rate
3. Macroscopic rate was greater than the microscopic rate.

This is illustrated in Figure 14. The first type of behavior is usually observed at relatively low crack growth rates. At higher crack growth rates conditions 1 and 2 are not observed. The large deviation of crack growth rates between the macro and micro rates in condition 3 can be explained by the presence of appreciable dimple rupture along with striation-producing fatigue propagation.

Electron fractograph analysis of spectrum loaded specimens indicates that when a fatigue striation is produced, it is the result of one cycle of stress. However, it has been observed that for both varying alternating and varying mean stresses, when the applied mean or alternating stress range changes abruptly from a high to a low level, there is a period (at least 10 cycles) during which the fatigue crack apparently
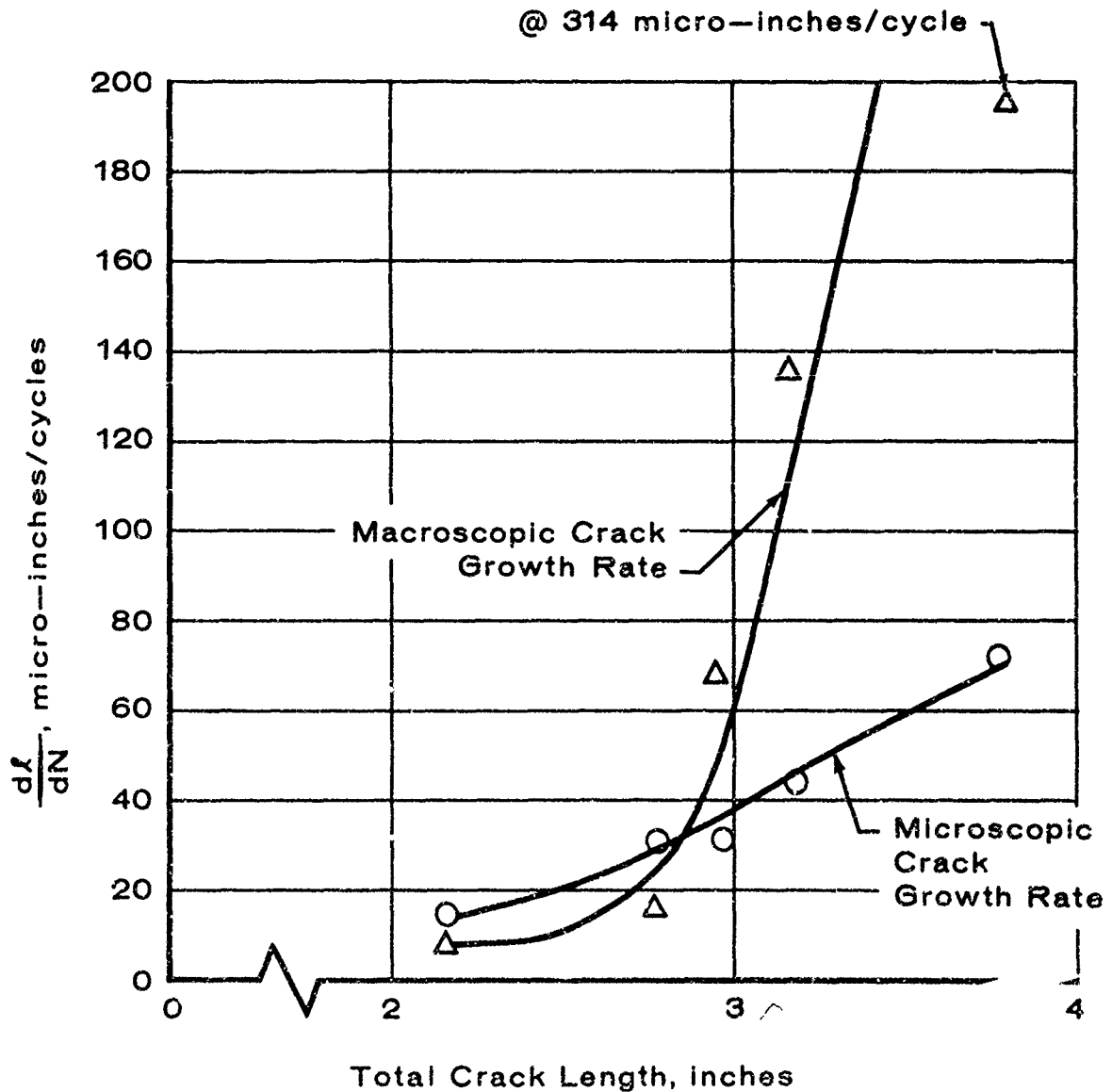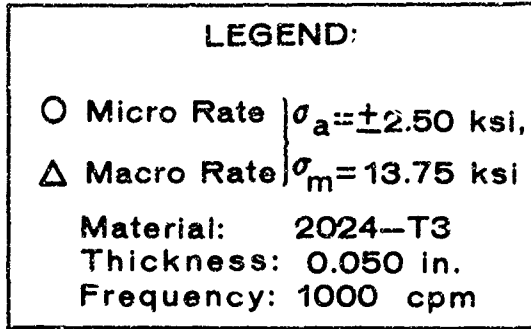
Figure 14.   Relationship Between Fatigue Microscopic and
Macroscopic Crack Growth Rate

does not propagate, Figure 15. On the other hand, when the low level is not immediately preceded by high levels of stress, fatigue crack propagation is observed.

The striation spacings were examined in terms of a parameter $K^{(5)}$ which describes the local intensity of stress in the vicinity of the crack tip, as:

$$K = \sigma \left[w \tan \left\{ \frac{\pi}{2w} \left(\ell + \frac{K^2}{\pi \sigma_y^2} \right) \right\} \right]^{1/2} \quad (1)$$

where σ = gross section stress

        w = panel width

        ℓ = total crack length

        σ_y = tensile yield strength

A representative plot of fatigue striation spacing, $d\ell/dN$, as a function of ΔK, $(K_{max} - K_{min})$, is shown in Figure 16. The dashed lines in the figure encompass the range of data points and suggest a relationship of the type:

$$\frac{d\ell}{dN} = \frac{(\Delta K)^4}{M} \quad (2)$$

This relationship is somewhat in agreement with previously published analyses [6, 7, 8]. However, examination of the figure reveals that the proportionality constant, M, is some complex function of the stress environment. For example, knowledge of $d\ell/dN$ alone from fractographic analysis will not define ΔK with satisfactory precision. A further
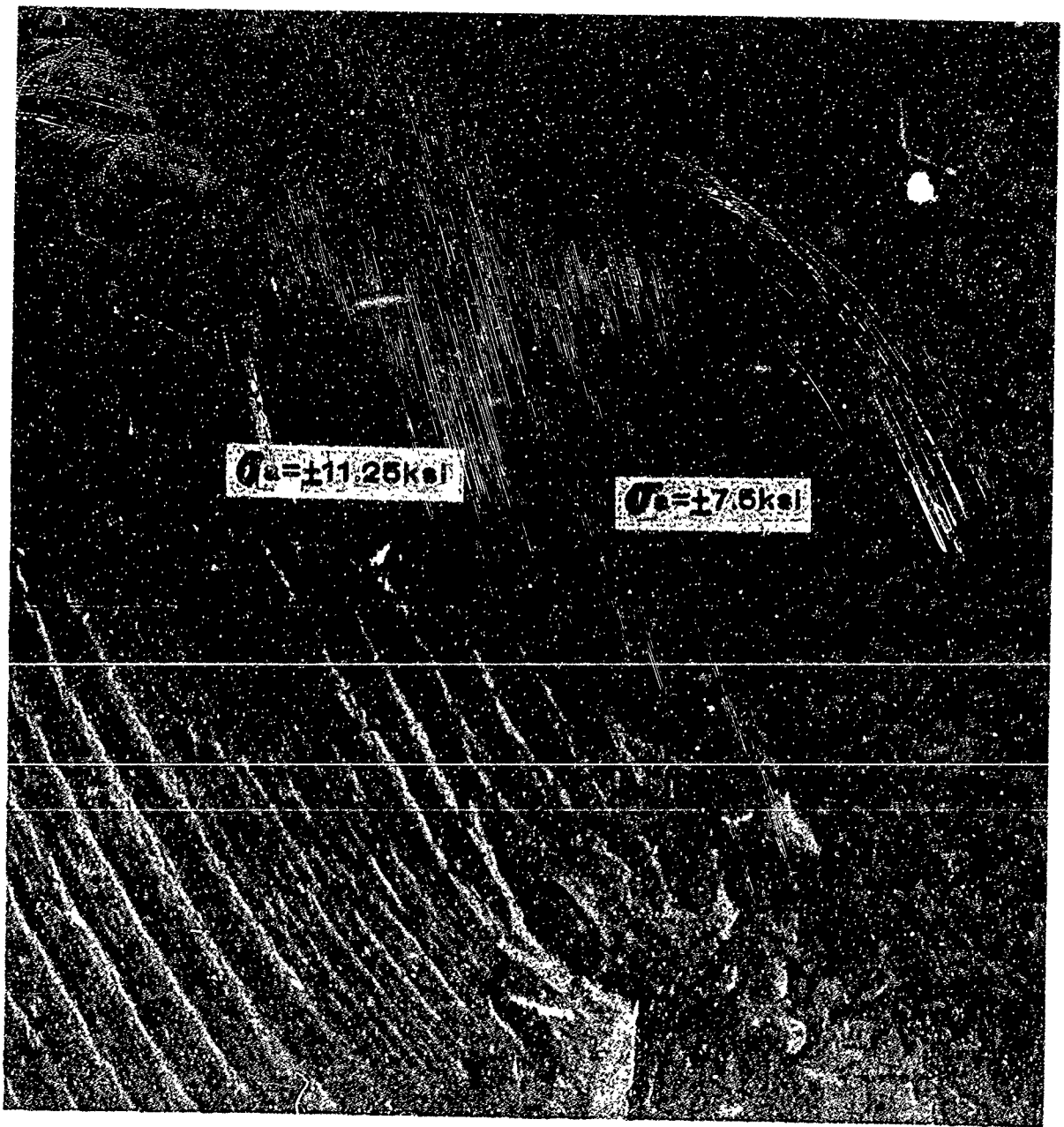
Magn. 13,800X

Figure 15.   Characteristics of Spectrum Loading.   Mean Stress =
            13.75 ksi, Three Alternating Stresses (2.5, 7.5 and
            11.25 ksi) Applied in 10 Cycle Intervals.   Note
            Lack of Striations for Lowest Alternating Stress
            (2.5 ksi).   Arrow Indicates Fracture Direction.
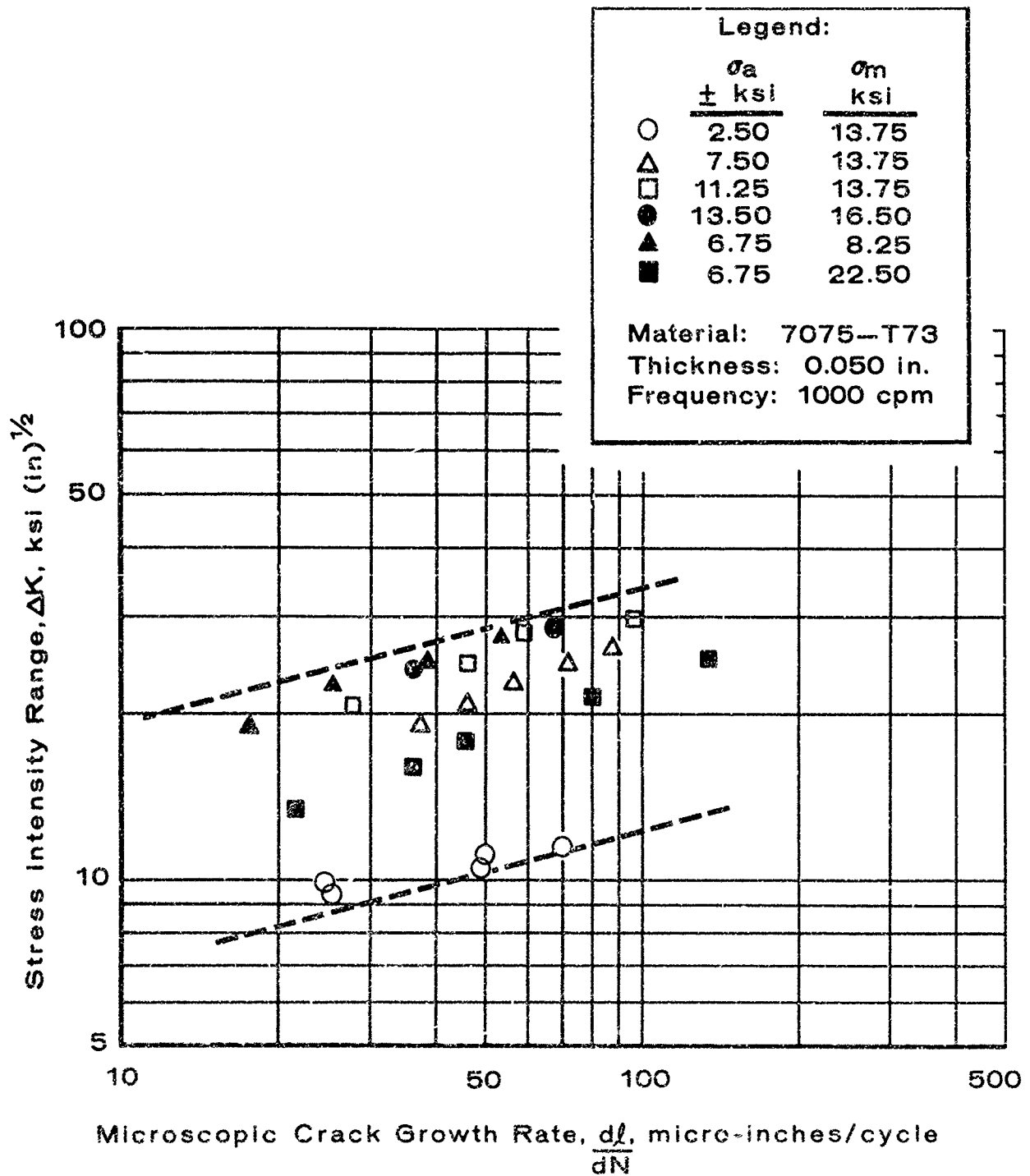
Figure 16. Relationship Between Striation Spacing and Stress Intensity Range Parameter ΔK

relationship between M and the stress environment must be known to make Eq. 2 useful as a correlation between striation spacing and stress environment.

When the range of the cyclic stresses under investigation is small, Eq. 2 will appear to define a correlation between ΔK and striation spacing (and between ΔK and macroscopic growth rate) and the proportionality constant, M, will have a discrete value.

When the range of cyclic stresses is expanded, however, as was true in this program as well as in Ref. 9, based on macro-rate, M is revealed as a multi-valued function of the stress.

For most aircraft structures the average mean stress is known (1-g load) and is generally constant for a given aircraft gross weight. Alternating stress, on the other hand, will vary and for many extreme operating conditions the magnitude of the alternating stress is not known. For this reason, striation spacings were examined with the objective of developing a correlation between alternating stress and the distance between fatigue striations.

Logarithmic plots of striation spacing, s, versus total crack length, ℓ, revealed that striation spacings increase with distance from the origin ($\ell/2$) as:

$$s = S_W \left(\frac{\ell}{W}\right)^m \tag{3}$$

where S_W = a constant depending on material, frequency and thickness

        m = a constant depending on the stress environment

        W = panel width

As shown in Figure 17 the slope, m, of the curves varies with the cyclic stress in such a manner that all curves intersect at a common point, (S_w, W). From this plot, however, the exact manner in which the cyclic stress influences the slope is not immediately obvious.

Further plots of the slope as a function of alternating stress at equal mean stresses, Figure 18, and as a function of mean stress at equal alternating stresses, Figure 19, indicated that the slope, m, can be described as:

$$m = p \, \sigma_a^{-1/2} \, \sigma_m^{-1/3} \tag{4}$$

where p is a constant nearly equal to 10, as shown in Figure 20. Solving for alternating stress,

$$\sigma_a = \left(\frac{p}{m \, \sigma_m^{1/3}} \right)^2 \tag{5}$$

From Eq. 3,

$$m = \frac{\log (s/S_w)}{\log (\ell/W)} \tag{6}$$

Substituting in Eq. 5,

$$\sigma_a = \left[\frac{p}{\sigma_m^{1/3}} \, \frac{\log (\ell/W)}{\log (s/S_w)} \right]^2 \tag{7}$$

Equation 7 relates alternating stress to striation spacing by means of two constants, p and S_w, which can be determined by test. Values for the aluminum alloys tested in this program are given in Table 5. The value of the constant, p, varies only slightly from alloy to alloy and does not appear to be affected by cyclic frequency. The
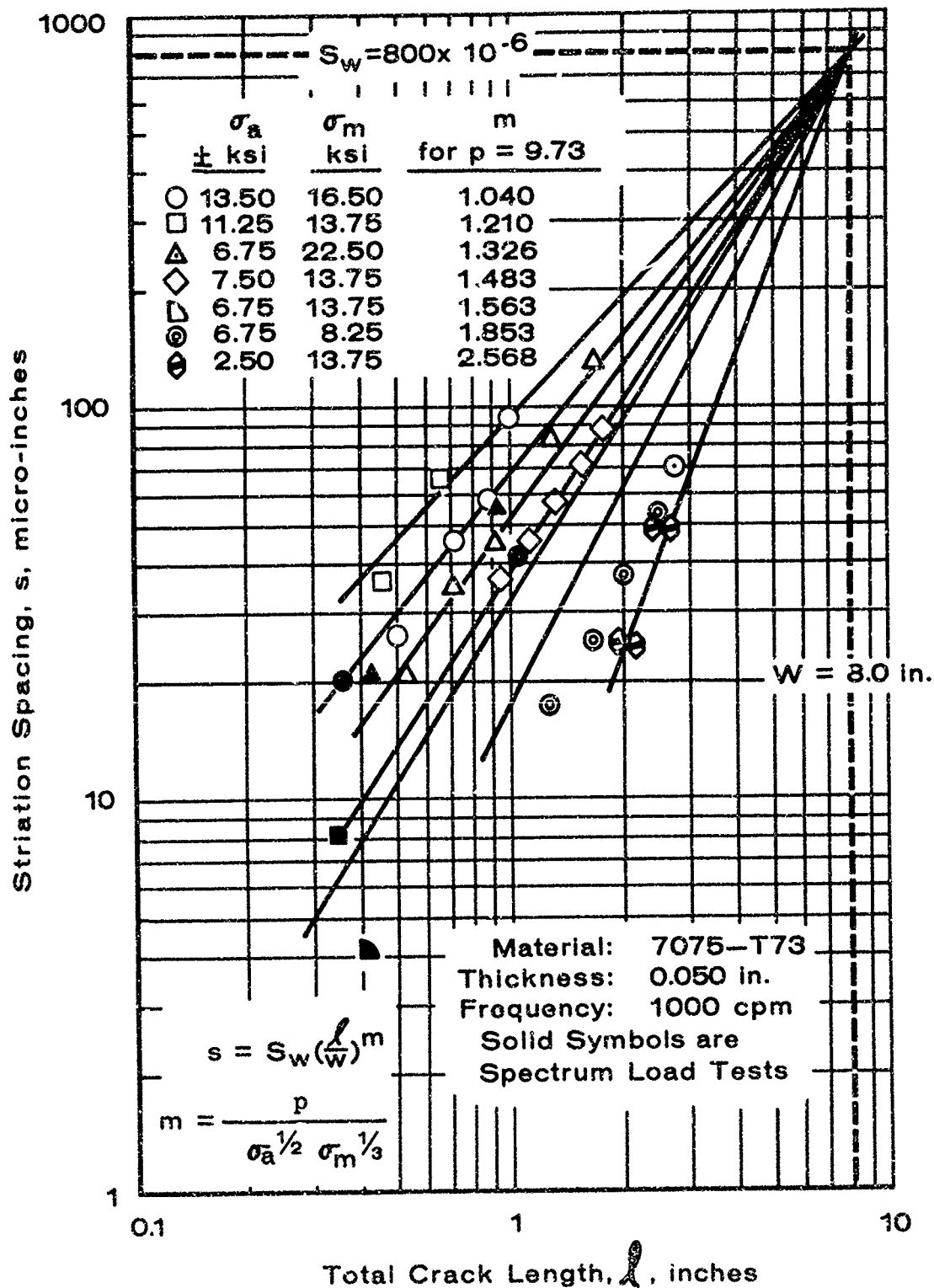
Figure 17. Striation Spacings Versus Crack Length
For 7075—T73, 0.050—in. Thick Panels
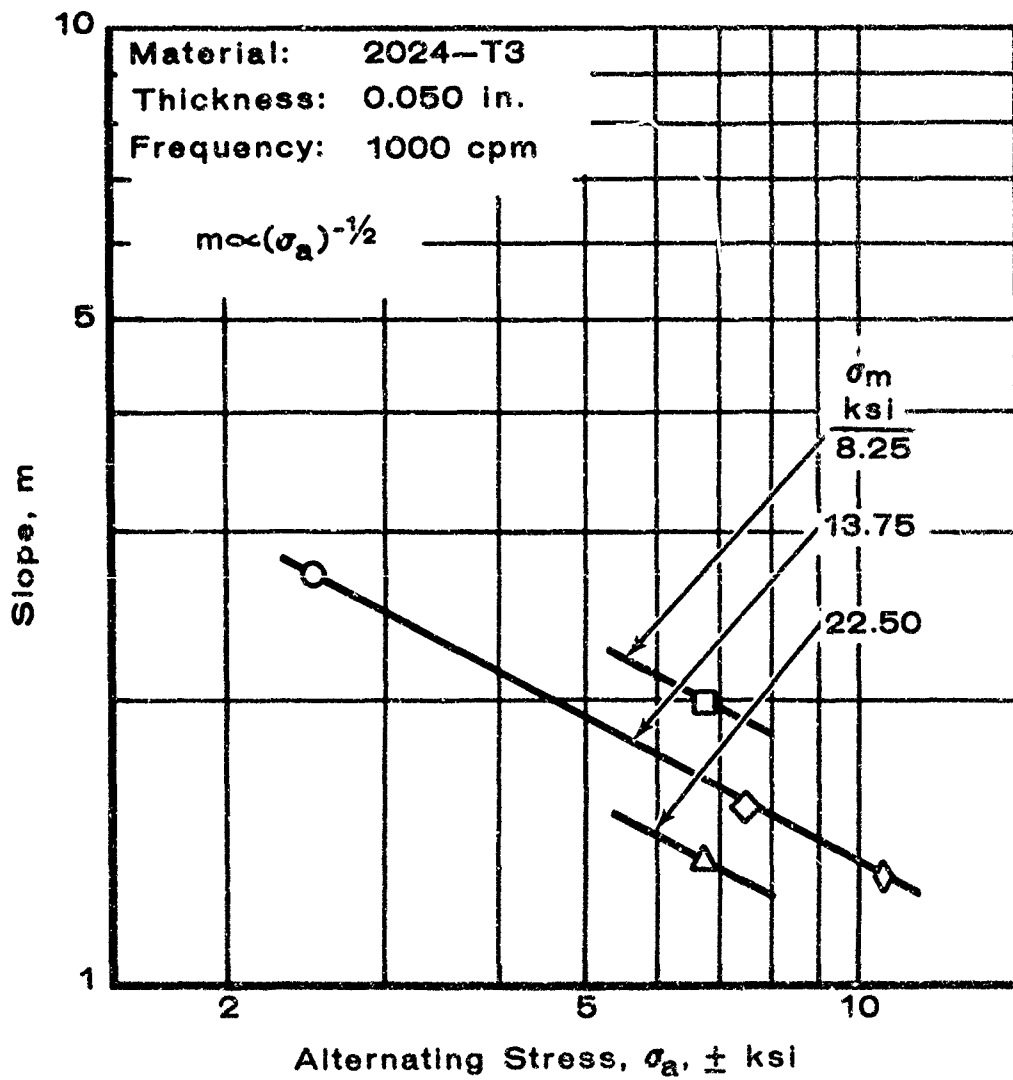
Figure 18. Effect of Alternating Stress on Slope, m
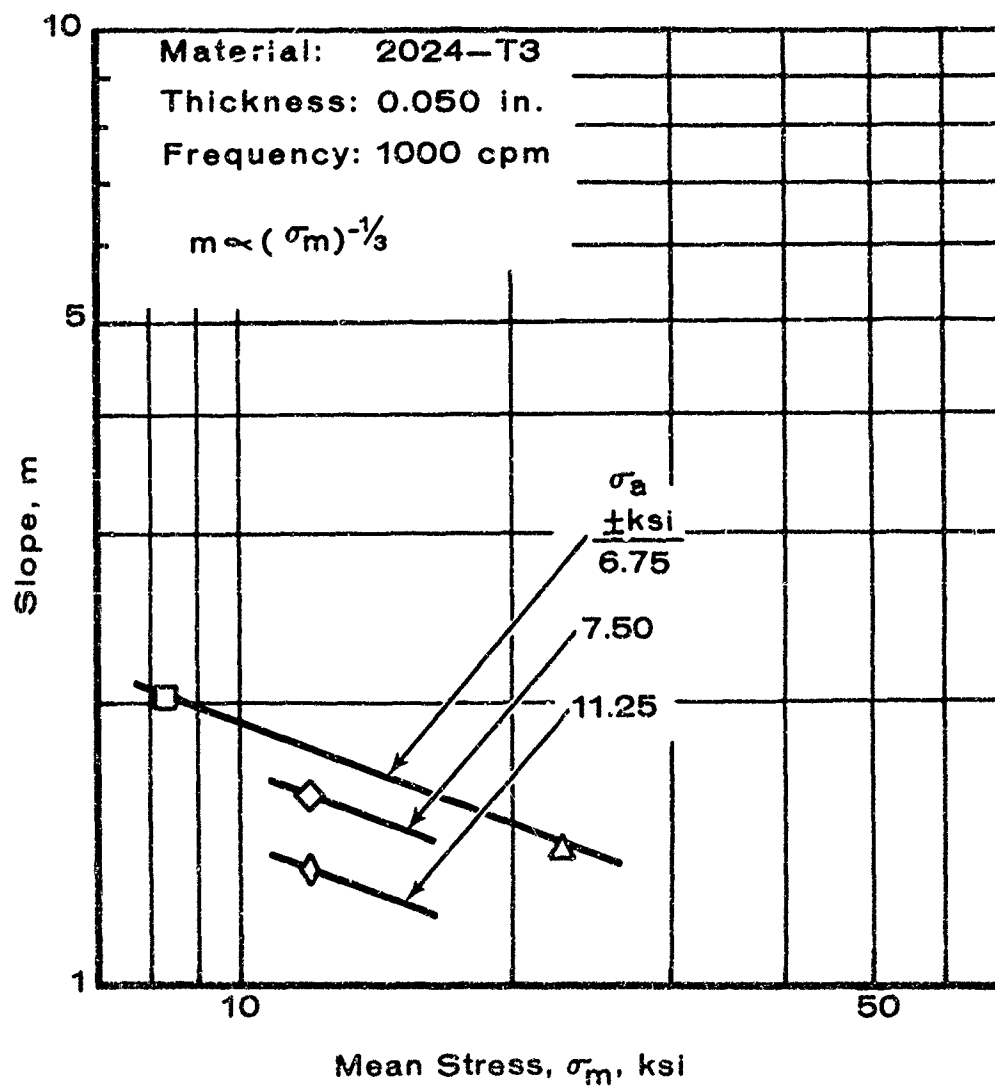
Figure 19. Effect of Mean Stress on Slope, m

The figure shows a log-log plot with:

- Y-axis: Slope, m (ranging from 1 to 10)
- X-axis: Mean Stress, σ_m, ksi (ranging from 10 to 50)

Annotations in the plot:

Material: 2024−T3
Thickness: 0.050 in.
Frequency: 1000 cpm

$$m \propto (\sigma_m)^{-1/3}$$

σ_a
±ksi
6.75
7.50
11.25
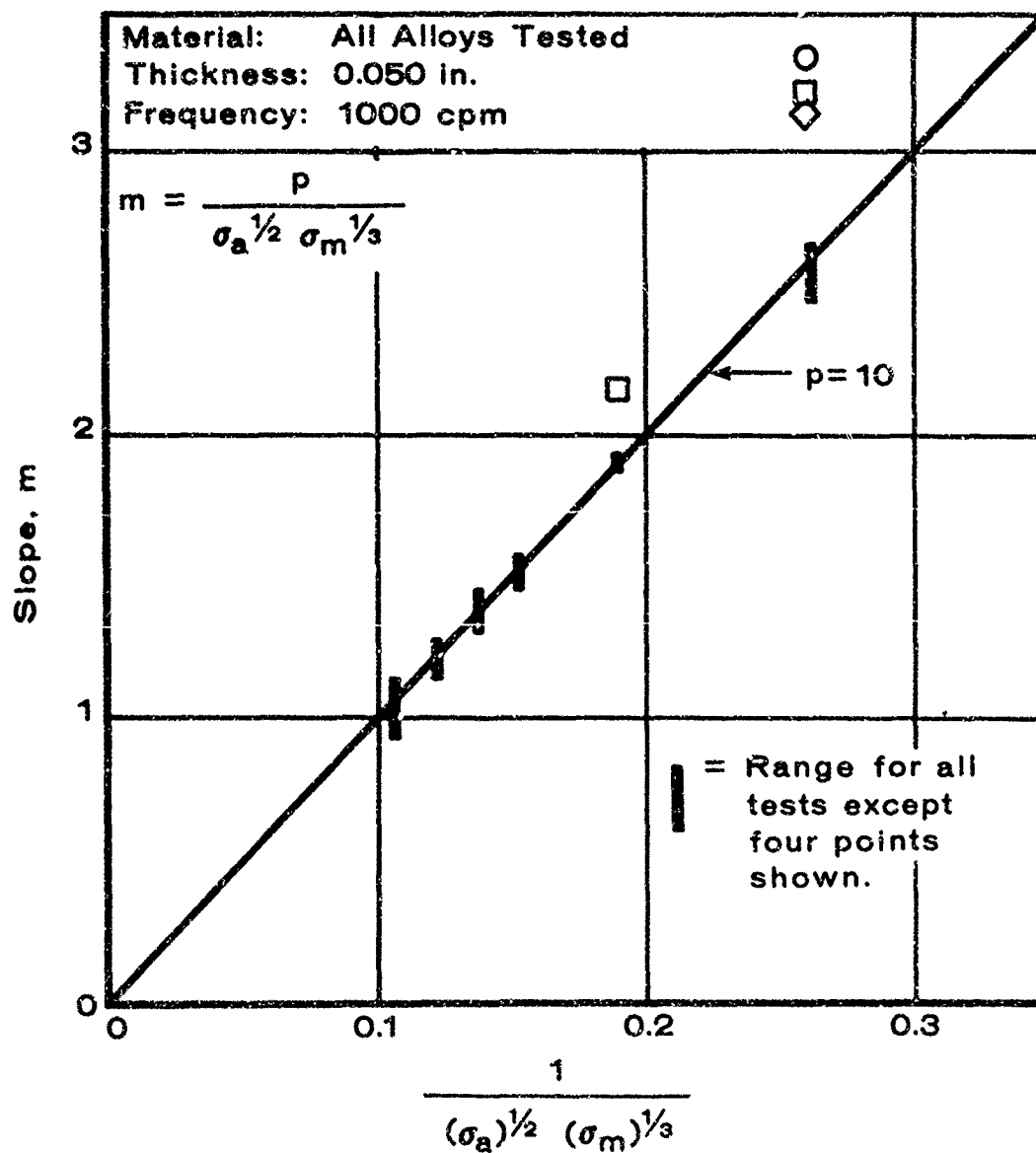
Figure 20. Determination of the Value of the Constant, p, in Eq. 3

TABLE 5—CONSTANTS FOR USE IN CORRELATING STRIATION
SPACINGS WITH CYCLIC STRESSES (EQ.7)

Material	Thick. in.	Frequency cpm	p (1)	s_w (2)
2024-T3	.050	1000	10.35	550×10^{-6}
		10	10.35	800×10^{-6}
	.500	1000	10.35	1500×10^{-6}
7075-T6	.050	1000	9.90	800×10^{-6}
		10	9.90	1000×10^{-6}
	.500	1000	--	---
7075-T73	.050	1000	9.73	800×10^{-6}
		10	9.73	1000×10^{-6}
	.500	1000	9.73	2000×10^{-6}
7079-T6	.050	1000	10.05	1000×10^{-6}
6061-T6	.050	1000	10.20	800×10^{-6}

(1)   Constant for Eq. 7 when σ_a and σ_m are in units of ksi

(2)   Constant for Eq. 7 when λ, W, and s are in units of inches

constant, S_w, varies more from alloy to alloy and shows a definite trend to increase with decreasing frequency and increasing thickness. An increase in S_w reflects larger striation spacing (higher crack growth rate).

All elements necessary to express the striation spacing, or crack growth rate, in terms of ΔK are present in Eq. 7. After the required substitutions and rearrangements, the resulting equation is somewhat cumbersome:

$$s = S_w \left[\frac{2}{\pi} \left\{ \text{arc tan} \left(\frac{\Delta K^2}{4\,\sigma_a\,W} \right) \right\} - \frac{\Delta K^2}{4W\pi\sigma_y^{\,2}} \right]^m \tag{8}$$

$$\text{where} \quad m = \frac{p}{\sigma_a^{\,1/2}\,\sigma_m^{\,1/3}}$$

Solution of this equation for alternating stress (upon which ΔK itself is dependant) is not convenient. However, it is interesting to note that the values of the exponent, m, experienced in this work varied from about 1.04 to 2.57. One indicated operation in Eq. 8 is the raising of ΔK^2 to the power of m, or the raising of ΔK to the power of 2m. For the values of m indicated above, the range of values for the exponent of ΔK is from 2.08 to 5 14. Reference 6 summarizes the work of various investigators who have found relationships of crack growth rate to ΔK raised to powers from 2 to 5.

The ability of Eq. 7 to describe the standard fatigue test data is demonstrated in Figure 21. In this figure, the alternating stress predi ted by Eq. 7 is plotted versus the actual alternating stress. Each data point in the figure represents the average predicted alternating
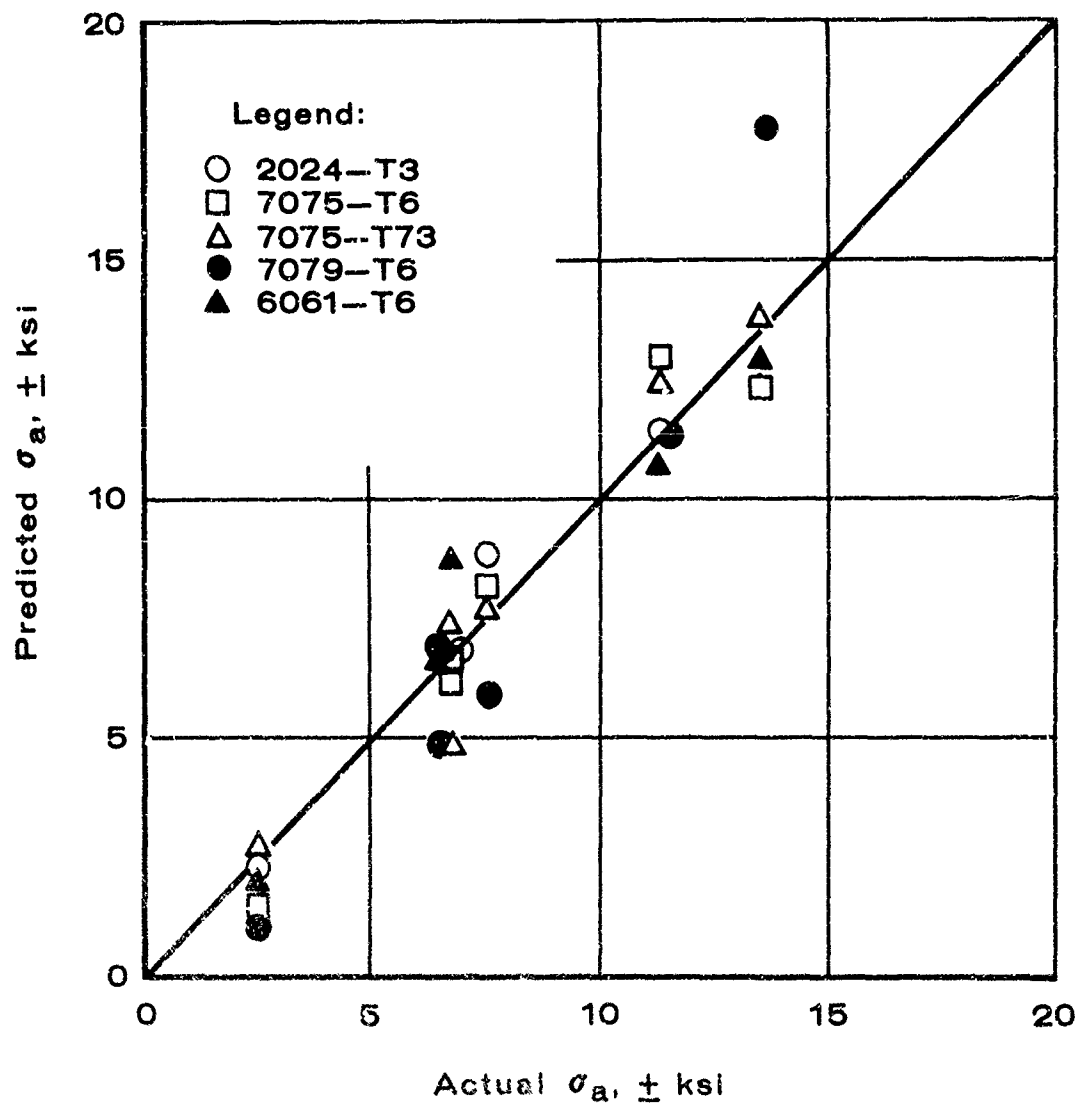
Figure 21. Comparison of Actual and Predicted Alternating Stress for 0.050-in. Thick Panels Fatigue Cracked at 1000 cpm

stress computed for each striation spacing measurement made in a given test. For most tests, the predicted value of alternating stress is within 1 or 2 ksi of the actual stress.

Predicted and actual alternating stresses for spectrum load tests are compared in Table 6 using the constants developed for a frequency of 1000 cpm.

Equation 7 can be employed in estimating the alternating stress for a given fatigue crack when the mean stress is known. To use the equation it is necessary to measure striation spacing, s, at a particular distance, $\lambda/2$, from the fatigue crack origin. A number of measurements at various distances will improve confidence in the results.

As an example, assume that a fatigue fracture from a 10 inch wide 7075-T73 structure operating at a mean stress of 18 ksi is to be analyzed to determine the maximum cyclic stress experienced during operation. Five striation spacing measurements are made at $\lambda/2$ distances from the origin. These $\ell/2$ distances are 0.5, 0.75, 1.0, 1.25, and 1.5 inches. Assume that the resulting striation spacings are 30, 56, 85, 115 and 150 micro-inches, respectively.

For the total crack length of 1.5 inches ($\lambda/2 = 0.75$) and the striation spacing of 56 micro-inches, the alternating stress is calculated as follows:

$$\sigma_a = \left[\frac{P}{\sigma_m^{1/3}} \frac{\log\,(\lambda/W)}{\log\,(s/S_w)} \right]^2$$

TABLE 6--COMPARISON OF ACTUAL AND PREDICTED ALTERNATING STRESS FROM SPECTRUM LOAD TESTS

Material	Mean Stress σ_m ksi	Actual Alternating Stress σ_a $\pm$ ksi	Average Predicted Alternating Stress σ_a* $\pm$ ksi
2024-T3	13.75	2.5 7.5 11.25	-- 7.86 16.30
	8.25 13.75 22.5	6.75	-- -- 6.46
7075-T6	13.75	2.5 7.5 11.25	-- 6.42 12.33
	8.25 13.75 22.5	6.75	-- 6.36 6.88
7075-T73	13.75	2.5 7.5 11.25	-- 7.52 10.18
	8.25 13.75 22.5	6.75	-- 5.31 8.24
7079-T6	13.75	2.5 7.5 11.25	-- 7.60 11.78
	8.25 13.75 22.5	6.75	-- 5.49 6.78
6061-T6	13.75	2.5 7.5 11.25	-- 6.24 11.82
	8.25 13.75 22.5	6.75	-- 8.24 7.72

* Calculated using Eq. 7 and constants from Table 5.

$$\sigma_a = \left[\frac{9.73}{(18)^{1/3}} \quad \frac{\log\left(\frac{1.5}{10}\right)}{\log\left(\frac{56 \times 10^{-6}}{800 \times 10^{-6}}\right)} \right]^2$$

$$= 7.01 \text{ ksi}$$

The results of calculations for the other crack lengths and striation spacings are shown in Table 7. The average calculated alternating stress is 7 ksi. Therefore, the maximum stress is

$$\sigma_{max} = \sigma_m + \sigma_a$$

$$= 18 \text{ ksi} + 7 \text{ ksi}$$

$$= 25 \text{ ksi}$$

TABLE 7--CALCULATED ALTERNATING STRESS FOR

IDEALIZED EXAMPLE GIVEN IN TEXT

Distance From Origin in.	Total Crack Length, in.	Striation Spacing micro-inches	Alternating Stress, σ_a ± ksi
0.50	1.00	30	6.78
0.75	1.50	56	7.01
1.00	2.00	85	7.10
1.25	2.50	115	7.04
1.50	3.00	150	7.13
		Average	7.01

Conclusions

1. The stress intensity range parameter ΔK does not satisfactorily describe the relationship between fatigue striation spacing and cyclic stress.

2. If one stress condition is known, such as mean stress, the empirical relationship

$$\sigma_a = \pm \left[\frac{p}{\sigma_m^{1/3}} \cdot \frac{\log(\zeta/W)}{\log(s/8_w)} \right]^{-2}$$

permits a reasonably accurate calculation of the magnitude of the other stress, i.e., alternating stress, in through-crack, thin sheet.

3. The reduction of fatigue frequency from 1000 cpm to 10 cpm results in an increase in the striation spacing at equivalent stress conditions.

4. An increase in thickness from 0.050 in. to 0.500 in., results in an increase in the striation spacing at equivalent cyclic stress and test frequency.

5. An abrupt decrease of applied fatigue stress can result in a period of arrested crack growth.

6. A fatigue striation is the result of one cycle of stress.

7. The appreciable difference between microscopic and macroscopic growth rates can be explained by the presence of dimple rupture areas on a fatigue surface.

8. Fatigue striations can be observed on both the normal and the oblique mode of fracture.

Acknowledgement

References

(1) "Handbook for Aircraft Accident Investigators", NAVAER 00-80T-67
U. S. Naval Aviation Safety Center, Office of the Chief of Naval
Operations, 1957.

(2) A. Phillips, V. Kerlins and B. V. Whiteson, "Electron Fractography
Handbook", AFML-TR-64-416, Air Force Materials Laboratory, Wright-
Patterson AFB, Ohio, January, 1965.

(3) C. B. Gilpin, D. H. Paul, S. K. Asunmaa and N. A. Tiner, "Electron
Distribution in Steel", Symposium on Advances in Electron Metallo-
graphy, Am. Soc. Testing and Mater. Spec. Tech. Publ. to be
published. Presented at Lafayett, Ind., June, 1965.

(4) A. R. Troiano, "The Role of Hydrogen and Other Interstitials on
the Mechanical Behavior of Metals", Trans., A.S.M. $\underline{52}$ (1960), p. 54.

(5) "Fracture Testing of High Strength Sheet Materials", ASTM Bulletin,
January and February, 1960.

(6) P. Paris and F. Erdogan, "A Critical Analysis of Crack Propagation
Laws", Journal of Basic Engineering, ASME, December, 1963.

(7) R. W. Hertzberg, "Application of Electron Fractography and Fracture
Mechanics to Fatigue Crack Propagation in High Strength Aluminum
Alloys", Lehigh University, 1965.

(8) J. M. Krafft, 'On Prediction of Fatigue Crack Propagation Rate from
Fracture Toughness and Plastic Flow Properties", Trans. ASM,
Vol. 58, 1965.

(9) D. A. Eitman and R. A. Rawe, "Plane Stress Cyclic Flaw Growth of
2219-T87 Aluminum and 5Al-2.5Sn Titanium Alloys", NASA CR-54956,
June, 1966.

APPENDIX I
MEASURED AND CALCULATED DATA FOR TASK C

Material and Spec. Code	Thickness, in.	σ_{mean}, ksi (1)	σ_{alt}, ± ksi (1)	Test Frequency CPM	Total Crack Length ℓ, in.	Striation (2) Spacing, μ-in.	No. Cycles per 0.1 in. Increments (4)	Macroscopic (3) Growth Rate, μin./cycle	K_{max}, ksi (in.)$^{1/2}$	ΔK ksi (in.)$^{1/2}$
2024-T3 (3-1)	0.050	13.75	2.5	1000	2.17	17.3	7,026	14.2	32.0	10.2
"	"	"	"	"	2.77	34.2	4,503	22.2	37.1	11.7
"	"	"	"	"	2.97	34.6	1,548	64.6	38.8	12.5
"	"	"	"	"	3.17	42.9	772	139.0	40.6	13.1
"	"	"	"	"	3.77	70.4	314	318.0	46.3	15.1
2024-T3 (3-2)	0.050	13.75	7.5	1000	1.02	25.5	3,353	89.9	28.4	20.4
"	"	"	"	"	1.22	35.4	1,845	54.1	31.2	22.4
"	"	"	"	"	1.42	51.9	993	101.0	33.8	24.3
"	"	"	"	"	1.62	53.5	640	156.0	36.3	26.1
2024-T3 (3-22)	0.050	13.75	11.25	1000	0.45	14.2	4,544	22.0	22.42	20.31
"	"	"	"	"	0.85	31.4	1,174	84.3	30.97	28.06
"	"	"	"	"	1.25	51.9	267	348.0	37.87	34.32
2024-T3 (3-18)	0.050	16.5	13.5	1000	0.36	31.5	1,008	109.0	24.4	22.?
"	"	"	"	"	0.56	55.5	585	171.0	30.5	27.7
"	"	"	"	"	0.06	74.4	101	990.0	40.2	36.5
2024-T3 (3-16)	0.050	8.25	6.75	1000	1.27	16.5	8,662	11.6	21.9	19.8
"	"	"	"	"	1.67	21.6	3,641	27.4	25.4	22.9
"	"	"	"	"	2.07	38.3	1,845	54.2	28.6	25.8
"	"	"	"	"	2.67	62.9	758	132.0	33.3	30.0
"	"	"	"	"	2.97	80.3	304	329.0	35.6	32.2
2024-T3 (3-17)	0.050	22.5	6.75	1000	0.51	9.8	10,041	10.0	28.7	14.2
"	"	"	"	"	0.71	18.5	5,188	19.3	33.9	16.8
"	"	"	"	"	0.91	26.7	3,372	29.7	38.5	19.1
"	"	"	"	"	1.11	42.9	1,820	55.0	42.8	21.3
"	"	"	"	"	1.31	60.9	877	114.0	46.8	23.3
2024-T3 (3-26)	0.050	13.75	7.5	10	0.93	33.4	2,396	39.2	27.3	19.6
"	"	"	"	"	1.33	62.9	1,078	93.0	32.9	23.6
"	"	"	"	"	1.73	75.5	608	164.4	37.8	27.2
"	"	"	"	"	2.13	114.1	464	215.8	42.6	30.7
2024-T3 (3-3)	0.050	13.75	11.25	10	0.52	33.8	3,384	27.9	24.1	21.9
"	"	"	"	"	0.72	49.2	1,754	57.0	28.4	25.8
"	"	"	"	"	0.92	63.7	1,115	89.6	32.3	29.2
"	"	"	"	"	1.22	76.3	672	149.0	37.4	33.9
"	"	"	"	"	1.42	104.3	257	359.0	40.3	36.8
"	"	"	"	"	1.62	120.8	190	526.0	43.6	39.5
2024-T3 (3-37)	0.50	13.75	2.5	1000	2.10	53.2	325	191.0	31.2	9.9
2024-T3 (3-38)	0.50	13.75	7.5	1000	0.89	60.2	915	109.2	26.3	18.8
"	"	"	"	"	1.09	116.1	368	279.0	29.1	20.9
2024-T3 (3-46) (Spectrum Load)	0.050	13.75 13.75 13.75	2.5 7.5 11.25	600	0.30 0.30 0.30	Not Observed 3.5 12.5	—	—	—	—
2024-T3 (3-51) (Spectrum Load)	0.050	8.25 13.75 22.5	6.75 4.75 6.75	600	0.46 0.46 0.46	Not Observed Not Observed 9.0	—	—	—	—

Notes:

(1) Based on gross area.

(2) Average of three or more readings over a 0.10 inch increment.

(3) Calculated by dividing the 0.10 inch incremental crack growth by the number of cycles used to propagate the crack through that increment.

Material and Spec. Code	Thickness, in.	σ_{mean}, ksi [1]	$\sigma_{alt.}$, ± ksi [1]	Test Frequency CPM	Total Crack Length l, in.	Striation (±) Spacing μ-in	No. Cycles for 0.1 in. Increment [2]	Macroscopic [3] Growth Rate, in./Cycle	K_{max} ksi (in.)$^{1/2}$	ΔK ksi (in.)$^{1/2}$
7075-T6 (3-4)	0.050	13.75	2.5	1000	1.95	7.8	8,572	11.7	29.6	9.9
"	"	"	"	"	2.15	11.6	6,539	15.3	31.3	9.0
"	"	"	"	"	2.35	17.7	5,950	16.8	32.9	10.3
"	"	"	"	"	2.55	18.8	3,667	25.8	34.5	10.8
"	"	"	"	"	2.75	21.2	3,376	42.6	36.2	11.3
"	"	"	"	"	2.95	23.6	2,517	39.8	37.8	11.9
"	"	"	"	"	3.15	25.1	627	159.0	39.5	12.4
7075-T6 (3-5)	0.050	13.75	7.50	1000	1.04	39.3	1,363	73.2	27.9	19.9
"	"	"	"	"	1.24	55.1	723	138.0	30.6	21.8
"	"	"	"	"	1.44	73.2	421	237.0	33.1	23.6
7075-T6 (3-6)	0.050	13.75	11.25	1000	0.54	37.0	1,435	69.6	23.8	21.4
"	"	"	"	"	0.74	49.6	1,047	95.6	27.8	25.1
"	"	"	"	"	0.94	75.9	291	344.0	31.5	28.4
"	"	"	"	"	1.14	82.2	239	347.0	34.8	31.4
7075-T6 (3-21)	0.050	16.50	13.50	1000	0.50	30.3	1,366	73.2	27.7	25.1
"	"	"	"	"	0.70	62.9	468	214.0	32.9	29.7
7075-T6 (3-19)	0.050	8.25	6.15	1000	1.24	23.2	3,089	32.4	21.4	19.3
"	"	"	"	"	1.64	38.9	1,594	62.7	24.8	22.3
7075-T6 (3-20)	0.050	22.5	6.75	1000	0.57	19.6	4,674	21.4	28.8	13.7
"	"	"	"	"	0.77	32.7	1,624	51.3	33.6	16.0
"	"	"	"	"	0.97	43.3	816	122	37.8	18.0
7075-T6 (3-33)	0.050	13.75	7.50	10	0.98	44.4	1,353	64.4	29.8	21.2
"	"	"	"	"	1.18	66.9	845	118.0	32.4	23.0
"	"	"	"	"	1.38	76.3	520	192.0	34.8	24.8
"	"	"	"	"	1.68	100.3	240	416.0	38.3	27.3
7075-T6 (3-34)	0.050	13.75	11.25	10	0.48	31.8	2,620	38.2	27.4	20.2
"	"	"	"	"	0.68	40.9	1,381	72.4	26.7	24.1
"	"	"	"	"	0.88	49.2	845	118.0	30.4	27.4
7075-T6 (3-41)	0.50	13.75	7.50	1000	0.72	49.9	187	534.0	23.1	16.5
7075-T6 (3-42)	0.50	13.15	11.25		0.43	26.3	1,097	52.7	21.2	19.1
"	"	"	"		0.63	55.9	861	116.0	23.6	23.2
7075-T6 (3-47) (Spectrum Load)	0.050	13.75	2.5	600	0.35	Not Observed	—	—	—	—
"	"	13.75	7.5	"	0.35	5.1	—	—	—	—
"	"	13.75	11.25	"	0.35	21.2	—	—	—	—
"	"	13.75	2.5	"	0.80	Not Observed	—	—	—	—
"	"	13.75	7.5	"	0.80	18.5	—	—	—	—
"	"	13.75	11.25	"	0.80	51.9	—	—	—	—
7075-T6 (3-52) (Spectrum Load)	0.050	6.25	6.75	600	.38	Not Observed	—	—	—	—
"	"	11.75	"	"	.38	3.5	—	—	—	—
"	"	22.50	"	"	.38	13.7	—	—	—	—

Material and Spec. Code	Thickness, in.	q_{max}, ksi [1]	$q_{alt.}$, ± ksi [1]	Test Frequency CPM	Total Crack Length $\bar{l}$, in.	Striation [2] Spacing, μ-in.	No. Cycles Per 0.1 in. Increment [4]	Macroscopic [3] Growth Rate, μ-in./Cycle	K_{max} ksi (in.)$^{1/2}$	ΔK ksi (in.)$^{1/2}$
7075-T73 (3-7)	0.050	13.75	2.50	1000	1.98	25.1	3,623	26.2	30.0	9.4
•	•	•	•	•	2.18	24.4	2,356	42.5	31.7	10.0
•	•	•	•	•	2.38	49.2	1,947	51.4	33.3	10.5
•	•	•	•	•	2.58	50.3	1,328	75.4	35.0	11.0
•	•	•	•	•	2.78	70.4	795	126.0	36.6	11.6
7075-T73 (3-8)	0.050	13.75	7.50	1000	0.94	37.4	2,823	54.8	26.7	19.0
•	•	•	•	•	1.14	45.2	1,277	78.3	29.5	21.0
•	•	•	•	•	1.34	55.6	879	114.0	32.1	22.9
•	•	•	•	•	1.54	72.2	639	157.0	34.6	24.7
•	•	•	•	•	1.74	87.7	272	368.0	37.0	26.4
7075-T73 (3-9)	0.050	13.75	11.25	1000	0.51	27.9	2,419	41.3	23.3	21.0
•	•	•	•	•	0.71	46.0	1,316	76.0	27.5	24.9
•	•	•	•	•	0.90	59.0	811	123.0	31.2	28.2
•	•	•	•	•	1.01	66.0	518	193.0	33.0	29.8
7075-T73 (3-24)	0.050	16.50	13.50	1000	0.45	36.2	1,887	33.0	26.7	24.2
•	•	•	•	•	0.65	66.9	829	121.0	32.1	29.1
7075-T73 (3-22)	0.050	8.25	6.75	1000	1.27	17.7	5,043	19.9	21.7	19.6
•	•	•	•	•	1.67	25.5	2,200	45.5	25.1	22.6
•	•	•	•	•	1.97	38.5	1,044	95.7	27.5	24.8
•	•	•	•	•	2.47	53.5	635	120.0	31.3	26.3
7075-T73 (3-23)	0.050	22.5	6.75	1000	0.52	21.6	4,029	24.8	27.9	13.4
•	•	•	•	•	0.72	36.6	2,144	46.6	32.9	15.9
•	•	•	•	•	0.92	56.0	912	110.0	37.3	18.0
•	•	•	•	•	1.32	82.6	483	207.0	45.1	21.8
•	•	•	•	•	1.72	133.8	254	394.0	52.0	25.2
7075-T73 (3-31)	0.050	13.75	7.50	10	0.95	37.7	2,066	48.4	26.8	19.1
•	•	•	•	•	1.15	51.9	1,579	63.3	29.6	21.1
•	•	•	•	•	1.25	73.5	786	127.0	31.0	22.1
•	•	•	•	•	1.55	107.8	485	206.0	34.7	24.8
7075-T73 (3-36)	0.050	13.75	11.25	10	0.43	22.0	2,752	36.4	21.4	19.3
•	•	•	•	•	0.63	52.3	1,702	58.7	25.9	23.4
•	•	•	•	•	0.73	57.8	947	105.5	27.9	25.2
•	•	•	•	•	1.13	114.1	330	303.0	34.9	31.6
7075-T73 (3-43)	0.50	13.75	2.50	1000	2.10	28.7	1,992	50.2	31.0	9.8
•	•	•	•	•	2.30	43.3	1,343	74.4	32.7	10.3
7075-T73 (3-44)	0.50	13.75	7.50	1000	0.92	73.5	898	111.0	26.5	18.9
•	•	•	•	•	1.12	96.0	526	190.0	29.3	20.9
•	•	•	•	•	1.32	119.4	294	340.0	31.9	22.8
•	•	•	•	•	1.72	148.8	131	764.0	36.8	26.3
7075-T73 (3-45)	0.50	13.75	11.25	1000	0.43	35.0	2,875	36.4	21.4	19.4
•	•	•	•	•	0.63	57.0	990	101.0	26.0	23.5
•	•	•	•	•	0.83	66.1	333	264.0	29.9	27.0
7075-T73 (3-48) (Spectrum Load)	0.050	13.75	2.50	600	0.35	Not Observed	—	—	—	—
•	•	•	7.50	•	0.35	7.8	—	—	—	—
•	•	•	11.25	•	0.39	21.6	—	—	—	—
•	•	•	11.25	•	1.04	43.7	—	—	—	—
7075-T73 (3-53)	0.050	8.25	6.75	600	0.41	Not Observed	—	—	—	—
•	•	13.75	•	•	0.41	4.3	—	—	—	—
•	•	22.5	•	•	0.41	22.4	—	—	—	—
•	•	22.5	•	•	0.90	59.2	—	—	—	—

Material and Spec. Code	Thickness, in.	S_{max}, ksi [1]	$S_{alt.}$, ± ksi [1]	Test Frequency CPM	Total Crack Length ℓ, in.	Striation [2] Spacing, μin.	No. Cycles Per 0.1 in. Increment ($\hat{c}$)	Macroscopic [3] Growth Rate, μin./cycle	K_{max} ksi (in.)$^{1/2}$	ΔK ksi (in.)$^{1/2}$
7079-T6 (3-10)	0.050	13.75	2.50	1000	1.99	10.2	7,539	13.2	30.7	9.5
"	"	"	"	"	2.39	16.1	5,473	18.3	33.4	10.5
"	"	"	"	"	2.99	25.9	3,856	26.0	36.4	12.2
"	"	"	"	"	3.49	33.4	1,953	51.2	42.8	13.6
"	"	"	"	"	4.29	68.5	547	182.5	50.7	16.3
7079-T6 (3-11)	0.050	13.75	7.50	1000	1.02	38.5	2,219	45.1	27.9	19.9
"	"	"	"	"	1.42	48.8	986	101.4	33.1	23.7
"	"	"	"	"	1.52	65.3	632	158.0	35.1	27.9
7079-T6 (3-12)	0.050	13.75	11.25	1000	0.46	30.7	2,483	40.2	22.1	20.0
"	"	"	"	"	0.66	45.4	1,054	94.8	26.5	24.0
"	"	"	"	"	0.85	63.3	640	156.0	30.4	27.5
"	"	"	"	"	1.26	93.7	367	273.0	37.0	33.5
"	"	"	"	"	1.66	145.6	144	695.0	42.9	38.8
7079-T6 (3-27)	0.050	16.50	13.50	1000	0.57	71.2	329	305.0	30.12	27.27
"	"	"	"	"	0.77	123.6	166	602.0	35.09	31.78
7079-T6 (3-25)	0.050	8.25	6.75	1000	1.23	30.3	3,054	32.8	21.4	19.3
"	"	"	"	"	1.63	40.5	1,782	56.1	24.8	22.4
"	"	"	"	"	2.33	55.9	954	105.0	30.3	27.3
"	"	"	"	"	3.23	79.5	321	312.0	37.8	33.6
"	"	"	"	"	3.53	118.1	175	572.0	39.7	35.8
7079-T6 (3-26)	0.050	22.50	6.75	1000	0.48	21.6	4,789	21.2	26.8	13.9
"	"	"	"	"	0.88	42.9	2,228	44.9	36.5	18.9
"	"	"	"	"	1.08	68.1	1,292	77.4	40.6	21.0
"	"	"	"	"	1.28	95.2	679	147.0	44.4	22.9
7079-T6 (3-49) (Spectrum Load)	0.050	13.75	2.50	600	0.42	Not Observed	—	—	—	—
"	"	"	7.50	"	0.42	11.4	—	—	—	—
"	"	"	11.25	"	0.42	27.5	—	—	—	—
7079-T6 (3-54) (Spectrum Load)	0.050	8.25	6.75	600	1.36	Not Observed	—	—	—	—
"	13.75	"	"	"		3.9	—	—	—	—
"	22.50	"	"	"		14.5	—	—	—	—
6061-T6 (3-13)	0.050	13.75	2.50	1000	1.95	9.0	7,972	12.5	30.6	9.9
"	"	"	"	"	2.35	18.1	4,617	21.6	34.1	11.1
"	"	"	"	"	2.75	26.3	3,054	32.4	37.7	12.4
"	"	"	"	"	3.15	36.6	2,105	47.5	41.4	13.7
"	"	"	"	"	3.35	44.8	916	109.0	43.3	14.4
"	"	"	"	"	3.85	69.6	582	172.0	48.7	16.6
6061-T6 (3-15)	0.050	13.75	11.25	1000	0.51	22.0	3,831	26.1	28.7	22.5
"	"	"	"	"	0.71	35.0	2,127	47.0	29.3	26.6
6061-T6 (3-30)	0.050	16.50	13.20	1000	0.48	35.4	1,905	52.5	30.3	27.7
"	"	"	"	"	0.68	51.1	839	119.0	36.2	33.1
6061-T6 (3-28)	0.050	8.25	6.75	1000	1.23	21.6	5,525	18.1	21.8	19.7
"	"	"	"	"	1.63	36.2	2,513	39.8	25.4	22.9
"	"	"	"	"	2.13	66.9	1,112	90.0	29.5	26.6
"	"	"	"	"	2.43	87.4	462	216	31.9	23.8
6061-T6 (3-29)	0.050	22.50	6.75	1000	0.42	23.2	6,691	15.0	27.3	14.1
"	"	"	"	"	0.92	58.2	4,031	24.5	40.9	21.1
"	"	"	"	"	1.32	89.3	1,123	82.0	49.7	25.8
6061-T6 (3-50) (Spectrum Load)	0.050	13.75	2.50	600	0.33	Not Observed	—	—	—	—
"	"	"	7.50	"	0.33	3.5	—	—	—	—
"	"	"	11.25	"	0.33	21.2	—	—	—	—
"	"	"	11.25	"	0.85	37.7	—	—	—	—
6061-T6 (3-55) (Spectrum Load)	0.050	8.25	6.75	600	0.35	Not Observed	—	—	—	—
"	"	13.75	"	"	0.35	6.6	—	—	—	—
"	"	22.50	"	"	0.35	22.0	—	—	—	—
"	"	22.50	"	"	3.53	45.2	—	—	—	—